Schweizerische Eidgenossenschaft
Confédération suisse
Confederazione Svizzera
Confederaziun svizra

Final report dated 22nd November 2021

Experimente und LES Wandwärmemodelle im Ottomotor

Experimentally Validated LES models for wall heat transfer in premixed charge spark ignition (Otto) engines

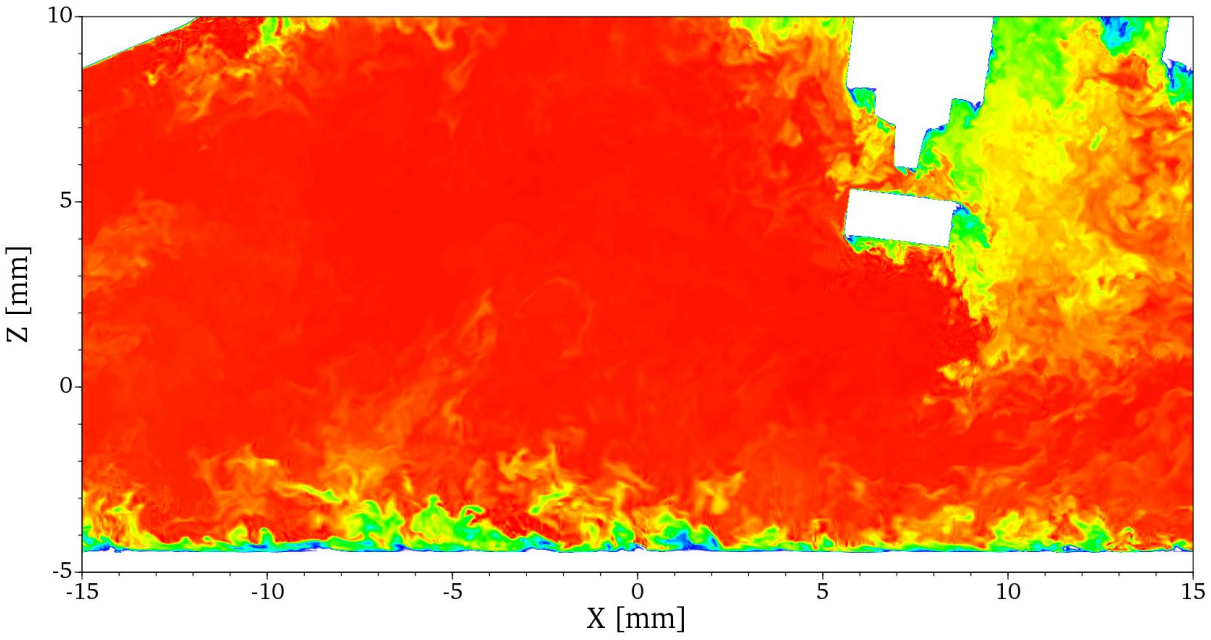

Date: 22nd November 2021

Location: Zurich, Switzerland

Subsidiser:
Swiss Federal Office of Energy SFOE
Energy Research and Cleantech Section
CH-3003 Bern
www.bfe.admin.ch

Co-financing
CORNET/FVV Project "Wall heat transfer II"

Subsidy recipients:
ETH Zürich
Institut für Energietechnik
Laboratorium für Aerothermochemie und Verbrennungssysteme
Sonneggstrasse 3
CH-8092 Zürich
http://www.lav.ethz.ch/

Authors:
Dr. Karri Keskinen, Aerothermochemistry and Combustion Systems Laboratory,
ETH Zürich, keskinen@lav.mavt.ethz.ch
Dr. George Giannakopoulos, Aerothermochemistry and Combustion Systems Laboratory,
ETH Zürich, georgeg@lav.mavt.ethz.ch
Dr. Michele Bolla, Aerothermochemistry and Combustion Systems Laboratory,
ETH Zürich, mbolla@lav.mavt.ethz.ch
Dr. Christos E. Frouzakis, Aerothermochemistry and Combustion Systems Laboratory,
ETH Zürich, frouzakis@lav.mavt.ethz.ch
Dr. Yuri M. Wright, Aerothermochemistry and Combustion Systems Laboratory,
ETH Zürich, wright@lav.mavt.ethz.ch
Prof. Konstantinos Boulouchos, Aerothermochemistry and Combustion Systems Laboratory,
ETH Zürich, boulouchos@lav.mavt.ethz.ch

SFOE project coordinators:
Dr. Carina Alles, Carina.Alles@bfe.admin.ch
Stephan Renz, info@renzconsulting.ch

SFOE contract number: SI/501930-01

Zusammenfassung

Der Wandwärmeübergang im Verbrennungsmotor hat einen grossen Einfluss auf den Wirkungsgrad, Emissionen und Lebensdauer von Motorkomponenten. Verbesserte Wandwärmeübergangsmodelle sind deshalb essenziell für prädiktive Computational Fluid Dynamics (CFD) Simulationsverfahren, anhand welcher die nächste Motorgeneration weiterentwickelt werden kann.

In diesem Projekt gelangten multi-parameter laserdiagnostische Verfahren am Labor für reaktive Strömungen und Messtechnik (RSM) der TU Darmstadt zur Anwendung, in Kombination mit hochgenauen, wandaufgelösten Large Eddy Simulationen (WRLES) sowie wandmodellierten Large Eddy Simulationen (WMLES, welche in der Motorentwicklung üblicherweise im Einsatz sind). Alle Simulationen wurden am Laboratorium für Aero-thermochemie und Verbrennungssysteme an der ETH Zürich durchgeführt. Die experimentellen und numerischen Verfahren ergänzen sich dabei hervorragend: Das Experiment liefert grosse Datenmengen über hunderte von Motorzyklen bei unterschiedlichen Betriebsbedingungen, wenngleich bei tieferer räumlicher und zeitlicher Auflösung, nur für einen kleinen Bereich des Brennraums und nicht für sämtliche thermochemischen Zustände. Die Simulationen kann hingegen die komplette Evolution aller Variablen vollaufgelöst darstellen, jedoch nur für wenige Zyklen und mit Limitierungen hinsichtlich der Betriebsbedingungen.

Basierend auf Erkenntnissen aus dem erfolgreich abgeschlossenen Vorläuferprojekt [1, 2] wurde das kombinierte Verfahren weiter entwickelt. Neue Prozessrechnungen mit GT-Power ermöglichten es, Randbedingungen für die wandmodellierte LES zu generieren. Die wandmodellierten Simulationsdaten wurden anschliessend anhand der experimentellen Daten validiert für ungedrosselten Betrieb bei 800 Umdrehungen sowie bei mittleren Drehzahlen (1,500 U/min). Im Laufe des Projekts wurden höheraufgelöste experimentelle Daten bei 2,500 U/min verfügbar, womit eine Validierung auch bei dieser motorisch deutlich relevanteren Drehzahl erfolgen konnte. Die wandmodellierten Simulationen wurden bei feineren Auflösungen von 0.75 mm durchgeführt und das im Vorgängerprojekt entwickelte Verfahren wurde angewandt, um Anfangsbedingungen zu generieren für die wandaufgelöste LES. Der Rechenaufwand für die wandaufgelöste LES – bei der höheren Drehzahl und ungedrosselt – entspricht etwa demjenigen der DNS im Vorläuferprojekt bei 800 U/min und gedrosseltem Betrieb.

Anhand der wandaufgelösten Simulationsdaten konnte überprüft werden, ob sich die Aussagen aus dem Vorgängerprojekt bzgl. Struktur der Wandgrenzschichten im Motor generalisieren lassen. Es zeigte sich, dass die Grenzschichten bei den höheren Drehzahlen und ungedrosselt stärker entwickelt sind als bei den tieferen Drehzahlen im gedrosseltem Betrieb, womit sie, im Mittel, idealen Wandmodellen deutlich näherkommen. Nichtsdestotrotz zeigen die wandnahen Geschwindigkeits- und Temperaturprofile dennoch Abweichungen gegenüber idealen Wandgrenzschichten und zwar in Funktion von Zeit, Ort und Betriebsbedingung, weshalb verbesserte Wandmodelle unumgänglich sind. Das im Vorläuferprojekt entwickelte algebraische Modell [3] sowie ein verbreitetes, bereits verfügbares Modell [4] wurden anschliessend anhand der "alten" DNS Daten sowie den "neuen" wandaufgelösten Daten getestet, mit guter globaler Vorhersagefähigkeit. Das algebraische Modell zeigte dabei ein besonders konsistentes Verhalten bei Variation der Betriebsbedingungen, zu unterschiedlichen Zeitpunkten und an verschiedenen Orten im Brennraum. Für den geschleppten Betrieb kann dem Modell gute prädiktive Fähigkeiten attestiert werden; auch bei Bedingungen, anhand welcher das Modell nicht entwickelt bzw. kalibriert wurde. Das algebraische Modell zeigte auch im reaktiven Betrieb qualitativ ein viel-versprechendes Verhalten, wenngleich keine Daten für eine quantitative Validierung zur Verfügung standen.

Zukünftige Vorhaben sollten deshalb verstärkt auf reaktive Bedingungen ausgerichtet sein, um Wandwärmeübergangsmodelle ausgiebig testen bzw. weiterentwickeln zu können. Dies trifft im besonderen Masse auf zukünftige synthetische Kraftstoffe zu, welche höhere (H_2) bzw. tiefere (NH_3) Reaktivität aufweisen, die sich auf die Flammenstruktur in Wandnähe, den Löschabstand und damit auch auf den Wandwärmeübergang auswirkt.

Abstract

Wall heat transfer in internal combustion (IC) engines strongly affects engine efficiency, pollutant emissions and component durability. Improved modelling capabilities offer the basis for predictive computational fluid dynamics (CFD) tools essential to the design of next-generation IC engines.

For this purpose, advanced multi-parameter laser diagnostics at the Institute for Reactive Flows and Diagnostics (RSM) at TU Darmstadt (TUD) were used conjointly with high-fidelity wall-resolved large eddy simulations (WRLES) and engineering-scale wall-modelled large eddy simulations (WMLES) at the Aerothermochemistry and Combustion Systems laboratory (LAV) of ETH Zurich. The experimental and computational techniques complement each other: the experiments provide large amounts of data for hundreds of cycles and at different conditions, albeit at lower spatial and temporal resolution, and only for part of the domain and thermo-chemical state, while computations can provide the complete evolution of the system state, but for a small number of cycles and limited conditions. In this project, an extended workflow based on the one developed in the previous project [1, 2] was established. New GT-Power process simulation models are developed, to generate data for the subsequent WMLES which is validated against existing experimental datasets at unthrottled conditions at low (800 RPM) and intermediate engine speed (1,500 RPM). With the advent of the new, optical experimental data at the highest engine speed of 2,500 RPM, the numerical platform is further validated at these industrially relevant conditions. Multi-cycle WMLES simulations for the new operating condition are carried out using a finer resolution (0.75 mm), and the previously established workflow is used to pursue a wall-resolved large eddy simulation (WRLES) using computational resources corresponding to the direct numerical simulations (DNS) of the previous project.

The high-fidelity WRLES data was generated with a spectral element solver and used to investigate the universality of the observations and modelling approaches established during the previous project [1]. The present WRLES simulation at high engine speed and load displays boundary layers that appear more developed than in the previous, low RPM condition. On average, wall laws following ideal trends are better suited to the new, high Reynolds number condition. However, the mean near-wall flow and temperature scaling still deviate from ideal trends as a function of time, space, and operating condition, signifying the need for more developed models. An established model [4] and an algebraic model developed during the previous project [3] were benchmarked in both the previous and new operating conditions, yielding good global correspondence. The performance of the algebraic model was particularly consistent between OPs, at different time instances and over different in-cylinder regions. This is a remarkable result as the model was generated using previous DNS data only at specific engine conditions and components. Hence, in the motored case, the results suggest good model applicability in conditions that deviate considerably from model training conditions. In the fired case, the algebraic model also shows promising qualitative behaviour, although no quantitative reference is available for comparison.

Further work is required in fired conditions to validate heat transfer models. This is particularly important in view of future fuels with considerably higher (H_2) or lower (NH_3) reactivity, affecting the flame structure, quenching distance and thereby also the wall heat transfer.

Main findings

- Enabled by a workflow involving optical engine experiments and multi-cycle simulations, a novel, high-fidelity wall-resolved LES has been carried out in a highly engine-relevant operating condition of 2,500 RPM and 0.95 bar intake pressure
- Engine boundary layers on the piston surface are more developed at higher load and RPM, and on average, a more favourable modelling target for standard wall models
- Boundary layer scaling changes between (a) spatial location, (b) crank angle, and (c) operating point. Hence, fruitful construction of wall functions based on this scaling is doubtful and advanced models are preferable
- The novel algebraic model developed during the previous project performs well in CFD computations for (i) operating conditions and (ii) in engine components that were not a part of its development. This suggests good predictive capability over a wide range of operating conditions in IC engines.

Contents

Abbreviations

AFR	Air-fuel ratio
ALG	Algebraic heat transfer model
ATDC	After top dead centre
BDC	Bottom dead centre
BL	Boundary layer
BTDC	Before top dead centre
CA	Crank angle
CFD	Computational fluid dynamics
CR	Compression ratio
DDES	Delayed detached eddy simulation
DNS	Direct numerical simulation
ETHZ	ETH Zürich
HT	Heat transfer
IC	Internal combustion
LAV	Aerothermochemistry and Combustion Systems Laboratory (ETH Zürich)
LES	Large eddy simulation
MI	Magnitude index
MPI	Message passing interface
OP	Operating point
PIV	Particle image velocimetry
PTV	Particle tracking velocimetry
PR	Plensgaard-Rutland heat transfer model
RI	Relevance index
RSM	Institute for Reactive Flows and Measurements (TU Darmstadt)
SME	Small and medium-sized enterprise
SGS	Subgrid-scale
TDC	Top dead centre
TUD	TU Darmstadt
VLS	Viscous length scale
WMLES	Wall-modelled large eddy simulation
WRLES	Wall-resolved large eddy simulation

q_w	Wall heat flux
Re	Reynolds number
s_L	laminar flame speed
s_T	turbulent flame speed
u	Velocity
T	Temperature
u_τ	Shear velocity
Δx^+	Scaled wall-tangential spacing
y^+	Scaled wall-normal spacing
δ_μ	Viscous length scale

μ	Molecular viscosity
μ_{sgs}	Modelled subgrid-scale viscosity
ν	Kinematic viscosity
ρ	Density

1 Introduction

Wall heat transfer in internal combustion (IC) engines affects strongly engine efficiency, pollutant emissions and component durability. Firstly, heat losses reduce engine thermal efficiency significantly. Therefore, the interest in strategies reducing heat losses over the combustion chamber walls is strong. Insulation materials based on ceramics, the so-called “swing coatings”, have regained interest due to new materials and coating strategies which have recently become available providing coatings with higher durability. Secondly, heat loss during flame-wall interactions leads to incomplete combustion, resulting in unburned hydrocarbons and CO formation in the boundary layer, which can contribute significantly to the tail-pipe emissions. Finally, wall heat transfer may result in high local component temperatures, which decrease component durability or can locally lead to pre-ignition which can lead to severe engine damage. All these effects become even more critical with the trend towards higher power density.

The aim of this project is to combine advanced multi-parameter diagnostic strategies and well-resolved large eddy simulations in order to obtain an in-depth understanding of wall heat transfer processes within Otto engines at high engine speeds and loads, and provide high-quality data for the validation of existing models in engineering CFD tools as well as for the development of improved CFD models for the development of efficient engines.

Improved modelling capabilities offer the basis for predictive computational fluid dynamics (CFD) tools essential to the design of next-generation internal combustion engines. For this purpose, advanced multi-parameter laser diagnostics at the Institute for Reactive Flows and Diagnostics (RSM) at TU Darmstadt (TUD) have been used conjointly with high-fidelity direct numerical simulations (DNS) and high-resolution large eddy simulations (LES) at LAV, ETH Zurich in a previous joint project, “Improved description of heat transfer from in-cylinder gases to combustion chamber walls in spark ignition premixed Otto engines” (OttoWallHeatXfer). The experimental and numerical techniques complement each other: the experiments provide large amounts of data for hundreds of engine cycles and at different conditions, albeit at lower spatial and temporal resolution compared to DNS and only for part of the domain and thermo-chemical state, while DNS provides the complete evolution of the system state. However, DNS is only practical for a few well-chosen representative conditions at low engine speeds and loads. The present project builds on the previous study documented in [1, 2] where a single (motored & fired) compression stroke was computed with DNS, with excellent agreement with experimental boundary layer measurements. The vast amount of data from these computations was utilised to characterise the boundary layers and to develOP A new, partially data-driven heat transfer model.

In the present project, the understanding from the detailed analysis of an operating condition at low engine speed and intake pressure was extended to engine-relevant conditions under both motored and fired operation. For the experimental characterization the velocity boundary layer is monitored near the piston wall and the core flow simultaneously to investigate their interaction. For this purpose, the most recent advances in time-resolved particle image velocimetry/particle tracking velocimetry are exploited. The multi-cycle wall-modelled LES (WMLES) performed in the CFD solver Star-CD is firstly validated against existing experimental data-sets at unthrottled conditions at low (800 RPM) and intermediate engine speed (1,500 RPM). In a second step, the new experimental data generated in this project at the highest engine speed of 2,500 RPM are used to benchmark the numerical platform at these industrially relevant conditions. The originally proposed work was extended in two directions: firstly, high-fidelity wall-resolved LES was performed using a spectral element solver. In addition, the Star-CD results were cross-validated against the Simcenter CCM+ CFD code. This provides unique insights to the temporal evolution of the processes associated with heat transfer from the gas to engine walls. In a third step, at fired conditions, combustion models are calibrated to match the experimentally observed combustion process and the impact of heat release on the flow and boundary layer evolution is studied towards complementing the experimental findings.

2 Procedures and methodology

The available extensive data from the OttoWallHeatXfer project for operating conditions OP A (800 RPM / 0.95 bar) and OP C (1,500 RPM / 0.95 bar) are used for the validation of multi-cycle LES simulations of the motored engine flow. The operating conditions are then extended to higher engine speeds. The measurement matrix includes a variation of engine speed and intake pressure to alter the time scale, thickness and the Reynolds number of the boundary layer. The full optical access needed for such detailed measurements of the boundary layer limits the maximum accessible engine speed to 2,500 RPM for wide open throttle. The flow velocities are measured by a combined Particle Image Velocimetry/Particle Tracking Velocimetry (PIV/PTV) approach using silicon oil droplets for seeding. A new state-of-the-art 4 Mpix high-speed CMOS camera is employed for detection, allowing for the extension of the detailed boundary layer measurements from a single measurement per cycle to crank-angle-resolved measurements to capture the temporal evolution of the flow. The 4 Mpix CMOS camera can access for the first time a measurement area of ~10-15 mm with spatial resolutions better than 100 µm allowing for the determination of the flow within and outside the boundary layer.

The numerical simulations at LAV/ETHZ employ the flow field solver Star-CD with the mesh motion plug-in es-ICE, broadly established for IC engine combustion modeling and extensively used at LAV to perform the wall-modelled large eddy simulations (WMLES). Multi-cycle WMLES are performed using various mesh resolutions to compute the evolution of the bulk flow field and boundary layers. The results are validated with the data provided from the experiments. A single cycle of the WMLES of the new operating condition is selected and a high-fidelity, wall-resolved LES (WRLES) is computed. Detailed wall modelling benchmarks are then made against this WRLES. The employed approaches include existing models designed for engines (e.g. [4]), in addition to a wall heat transfer model developed during the previous project [3]. For fired and fully premixed engine operation methane is injected into the intake duct one meter upstream of the intake valves, and the impact of wall modelling on the fired process is investigated in a qualitative manner.

2.1 Workflow

The computational work at LAV employs both engineering-scale and high-resolution wall-resolved large eddy simulations (LES), while overlapping optical measurement data is prepared at the Institute for Reactive Flows and Diagnostics (RSM) at Technische Unversität Darmstadt (TUD). The different work packages and their interactions are graphically presented in Figure 1. Table 1 displays the new operating condition (OP E) targeted within the project.

Follow-up project "*Experimentally Validated LES models for wall heat transfer in premixed charge Otto engines*": extend findings to engine-relevant conditions

WP6 (TUD)	WP7 (ETHZ)
• Setup 2D2C high-speed PIV • Visualise flame front (Mie-scattering) • Characterise outer flow region and its influence on the BL • Examine locations with non-parallel wall flow	• Build model for high engine speeds • Validate against experiments • Examine universality of findings from ongoing project • Assess novel modelling approaches

Table 1. The new operating condition E

	0.95 bar	**0.4 bar**
800 RPM	A	B
1500 RPM	C	D
2500 RPM	**E (NEW)**	

The present work follows a step-by-step process summarised in Figure 2 in order to extend the observations of the previous project towards higher engine speed, unthrottled conditions that are highly relevant for the engine manufacturers. As a first rather straightforward step, the existing experimental conditions (OP A, OP C) are computed with WMLES using Star-CD. For this purpose, GT-Power process models are calibrated to the existing intake and exhaust pressure and temperature data. The calibrated models are then extended to the new OP, and preliminary multi-cycle computations are carried out with WMLES.

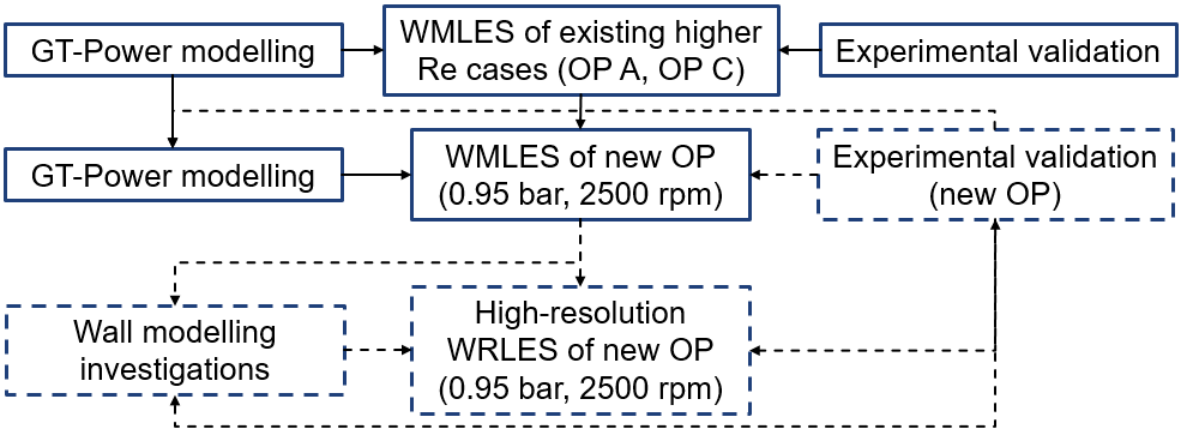

Figure 2. Computational workflow for non-reactive computations in the follow-up project.

Once data from measurements from RSM became available for the new OP, the calibration of the GT-Power models were further ascertained, and the multi-cycle WMLES can be compared with the particle image velocimetry PIV data.

High-fidelity data are generated by performing a wall-resolved LES with the Nek5000 code employed in the DNS in the first project. This component was not proposed in the original project plan, but adds significant value to the project since it provides (1) detail outside the reach of experiments, and (2) the ability to directly investigate wall heat transfer (in addition to momentum boundary layers). Filtering/stabilisation techniques recently benchmarked for the high-resolution wall-resolved LES (WRLES) of engine flows [5, 6] are employed in these new computations in order to keep the computational cost similar to the previous DNS, i.e. in the order of one million CPU hours. First, it is however important to determine whether the scaling of near-wall flow physics feasibly allows for reaching wall-resolved LES criteria.

Wall models are studied in several ways: 1) The output of optical measurements and WRLES simulations can be compared against existing correlations, 2) model formulations can be tested in detail against the WRLES simulations, and statistically against the experiments

2.2 Numerical methodology

The wall-resolved LES (WRLES) was performed with the code that has been co-developed by LAV at ETH Zurich and the Argonne National Laboratory (ANL) based on the open source, spectral element, incompressible flow solver Nek5000 [7]. The base code is the one employed in previous DNS [8]. Additionally, the present work benefits from prior experiences in carrying out WRLES with Nek5000 [5]. A filter-based stabilization method based on [6] is employed in the present work.

The spectral element method is a high-order weighted-residual technique that combines the efficiency of global spectral methods with the geometric flexibility of finite element methods to accurately represent and simulate complex geometries. Locally, the mesh is structured, with the data and geometry expressed as sums of high-order tensor product polynomials [9]. A high-order splitting scheme for low Mach number reactive flows [10] is used, separating the equations in the “thermochemistry" part (species and energy conservation equations) and the “hydrodynamic" part (continuity and momentum equations). The low Mach number formulation allows for time integration steps that are about an order of magnitude larger than fully-compressible. Nek5000 utilizes scalable domain-decomposition-based iterative solvers with efficient preconditioners. The parallel implementation is based on the standard message-passing Single Program Multiple Data mode, where contiguous groups of elements are distributed to processors and the computation proceeds in a loosely synchronous manner; communication is based on the Message Passing Interface (MPI) standard. The code exhibits very good parallel efficiency and scalability to over 1,000,000 processes on the most recent parallel architectures [7]. The Arbitrary Lagrangian-Eulerian (ALE) formulation allows for the accurate simulation of the piston motion [11].

The flow field solver STAR-CD with the mesh motion plug-in es-ICE, broadly established for IC engine combustion modelling, was used to perform the WMLES. A new wall model developed in the previous project and published in [3] has been implemented in STAR-CD via user-coded subroutines. Additionally, the newer Simcenter CCM+ code is used as a means of cross-validation. Similarly, for explorative fired simulations, user-coded combustion models with improved models for turbulent flame speed have been implemented in the existing G-equation (level-set) context.

3 Results and discussion

3.1 Improvement of GT-Power process simulation models

In order to provide pressure and temperature boundary conditions for the multi-cycle LES computation at the new operating point (OP E), updated GT-Power process simulation models were generated. Improvements with regard to previous work [8] included

- Updated valve timing estimates based on valve lift measurements carried out at TUD. The impact is a minor advance of 2 CAD. Within the measurement, there is some uncertainty of the valve lifts close to valve opening/closing.
- A combined target optimisation of temporal intake, cylinder and exhaust pressure traces, as well as average gas temperatures at the intake and exhaust measurement locations.
- Model optimisation as before by adjusting the in-cylinder heat transfer coefficient. In addition, both intake and exhaust wall temperatures have been adopted as input variables, to take into account uncertainty in the experiments.
- A slight adjustment of the length of the long intake pipe is mandated by the newly adjusted temperature boundary conditions, which lead to phasing differences in comparison to the existing models. This adjustment is justified by the form of the intake pipe construction, which includes a bend and an embedded multi-orifice nozzle – hence, evaluation of the effective length of such a flow connection is non-trivial.

The third point was found to be important in order to be able to closely match temperatures at the boundary locations. Figure 4 shows an example of such a result for OP C (a more detailed discussion can be found in our recent publication [12]). In general, the match between the profiles is very accurate, both in terms of the phasing and magnitude. For reference, Figure 3 displays the locations of the relevant boundary regions (magenta surfaces). To first test the dynamic capability of the tuning, the same set of parameters was applied to OP A (Figure 5).and resulted in a good agreement apart from minor differences in the mean temperature. Some temperature variation between different engine speeds (flow rates) should be expected.

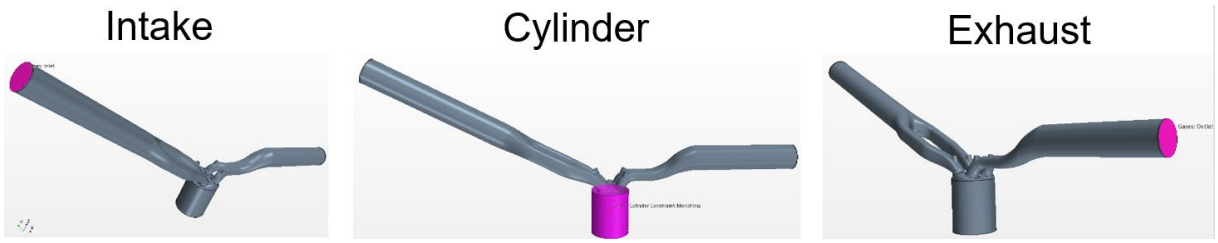

Figure 3. Physical locations of regions that function as the basis for GT-Power model tuning.

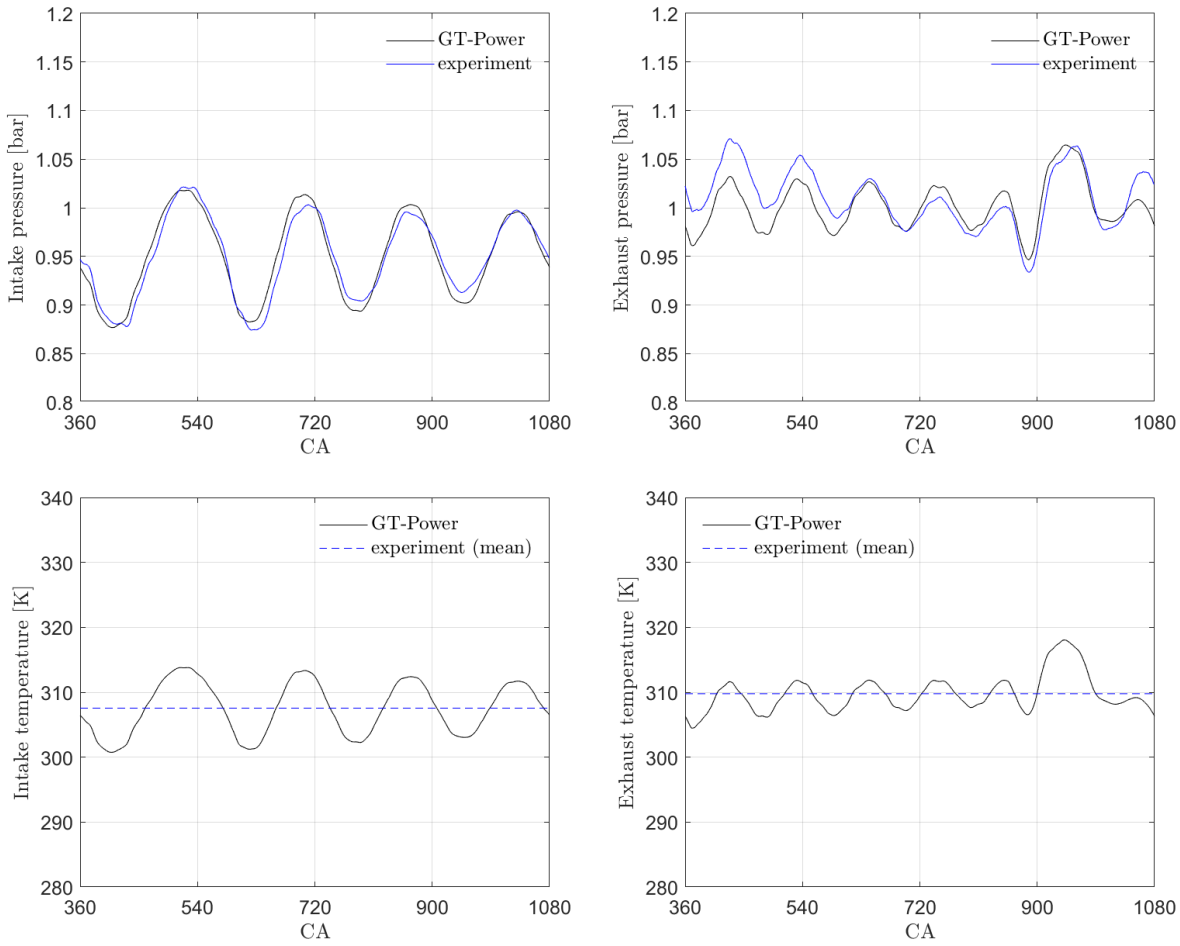

Figure 4. OP C (1500 RPM / 0.95 bar). Intake (left) and exhaust (right) pressures (top) and temperatures (bottom) in the GT-Power simulations and experiments

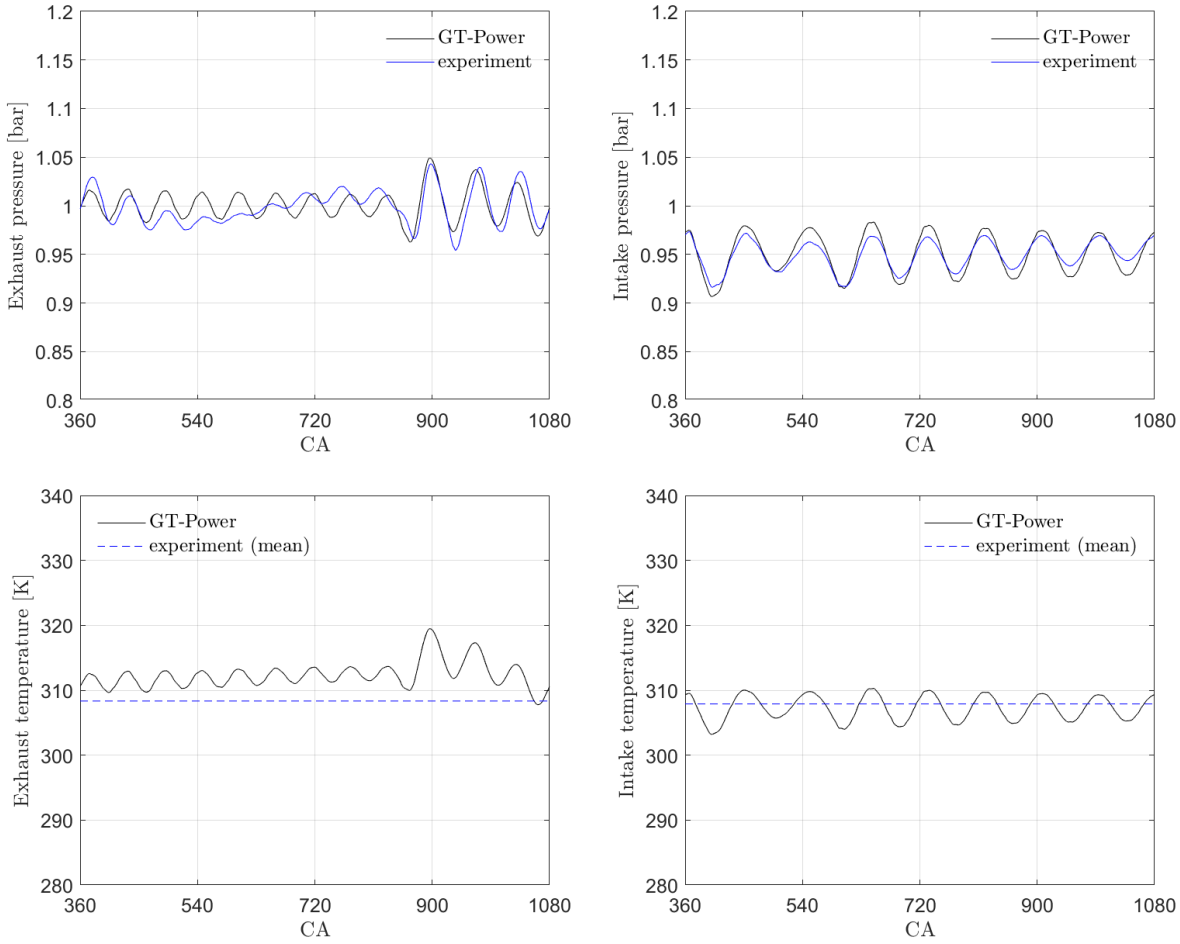

Figure 5. OP A (800 RPM / 0.95 bar). Intake (left) and exhaust (right) pressures (top) and temperatures (bottom) in the GT-Power simulations and experiments. For this dynamic test case, simulation settings were adopted from the OP C setup (Figure 4).

Results for the new operating condition (OP E) are displayed in Figure 6. It is notable that the higher engine speed causes the physically similarly scaled fluctuations to be slower with regard to crank angles. Furthermore, the magnitude of fluctuations is in general quite high, up to almost 0.4 bar in exhaust pressure. It is hence important to ensure that the fluctuations can be accurately represented by the GT-Power model. In contrast to Figure 5, the results in Figure 6 are from a model already incorporating the measurement data of OP E in the calibration.

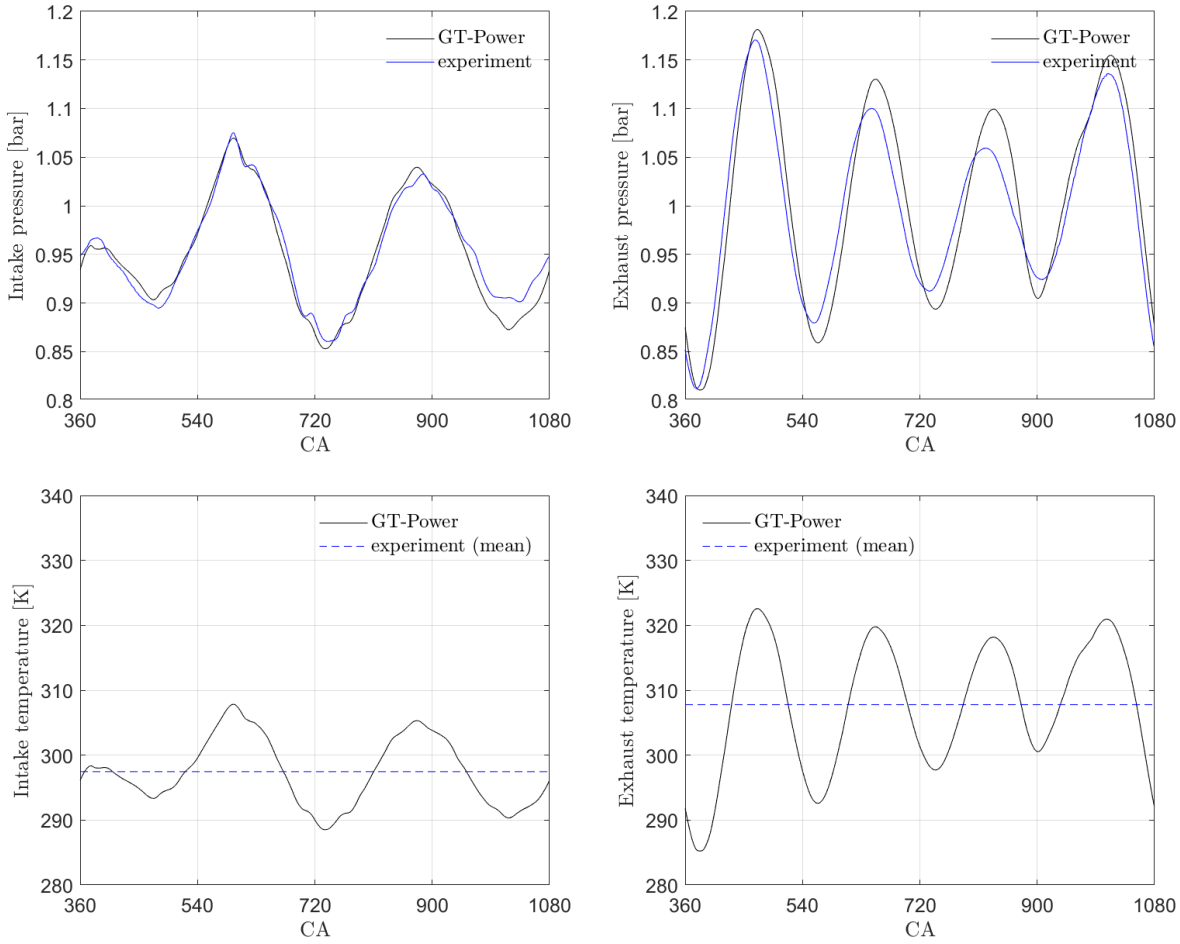

Figure 6. OP E (2500 RPM / 0.95 bar). Intake (left) and exhaust (right) pressures (top) and temperatures (bottom) in the GT-Power simulations and experiments.

3.2 Towards the new operating condition at 2500 RPM and 0.95 bar (OP E)

The multi-cycle WMLES computations have been primarily carried out with Star-CD with the modelling specifications summarised in Table 2:

Table 2. Numerical specifications in the WMLES computations.

Flow Field Solver	STAR-CD v4.30 by Siemens PLM
Mesh Motion	es-ICE plugin: cell layer addition / removal
Spatial discretization	2nd order MARS scheme
Time integration	Euler implicit
Time step size	0.04-0.125°CA
Pressure / Velocity coupling	PISO
Turbulence Model	transported k_{sgs}
Near-wall treatment	Plensgaard-Rutland model [4]
Species properties	Extended NASA polynomials
Initial & boundary conditions	Transient p/T from calibrated GT-Power simulations

3.2.1 Monitoring the experimental correspondence of multi-cycle LES at different OPs

Along the span of the Reynolds number index (shown below in Figure 15), OP A and OP C form convenient intermediate points between OP B (lowest Reynolds number, investigated in the previous project) and OP E (highest Reynolds number, the ultimate target of the present project). It is therefore interesting to observe how the correspondence between simulations and experiments change at different operating conditions. As an example, Figure 8 displays an example of mean flow comparisons between the present CFD work and the PIV experiments at TU Darmstadt. The metrics utilised here are the relevance (RI) and magnitude (MI) indices, which denote the correspondence between the orientation of vector fields [13, 14]

$$RI = \frac{\langle u_{i,CFD} \rangle \cdot \langle u_{i,EXP} \rangle}{\left\| u_{i,CFD} \right\| \cdot \left\| u_{i,EXP} \right\|} \tag{1}$$

$$MI = 1 - \frac{\left\| \langle u_{i,CFD} \rangle - \langle u_{i,EXP} \rangle \right\|}{\left\| u_{i,CFD} \right\| + \left\| u_{i,EXP} \right\|} \tag{2}$$

These metrics, operating on the velocity vector field, indicate the local correspondence between the computation and the experiment. The scaled dot product RI is constrained between -1 and 1, whereas $\leq MI \leq 1$. RI measures the local angles between the two vector fields, as an indicator of how well the orientation of the computational and experimental vector fields match. In contrast, MI measures the difference in both angle and magnitude, and is a more stringent metric.

As a baseline for comparisons, Figure 9 shows the collated phase-averaged mean flow correspondence between the scale-resolving delayed detached eddy simulation (DDES) and PIV measurements from the previous project [8]. The mean flow in the simulation was computed over 25 cycles, as opposed to 73 cycles in the experiment. The correspondence metrics however experience little change after about 10 cycles (Figure 7). Both RI and MI are averaged through the measurement domains in (a) spark, and (b) valve planes. To give an impression of a suitable range for RI and MI values in existing studies, Buhl et al. [13] report RI values between 0.7 and 0.95, and MI values between 0.6 and 0.85 in a piston top-oriented plane during the intake stroke.

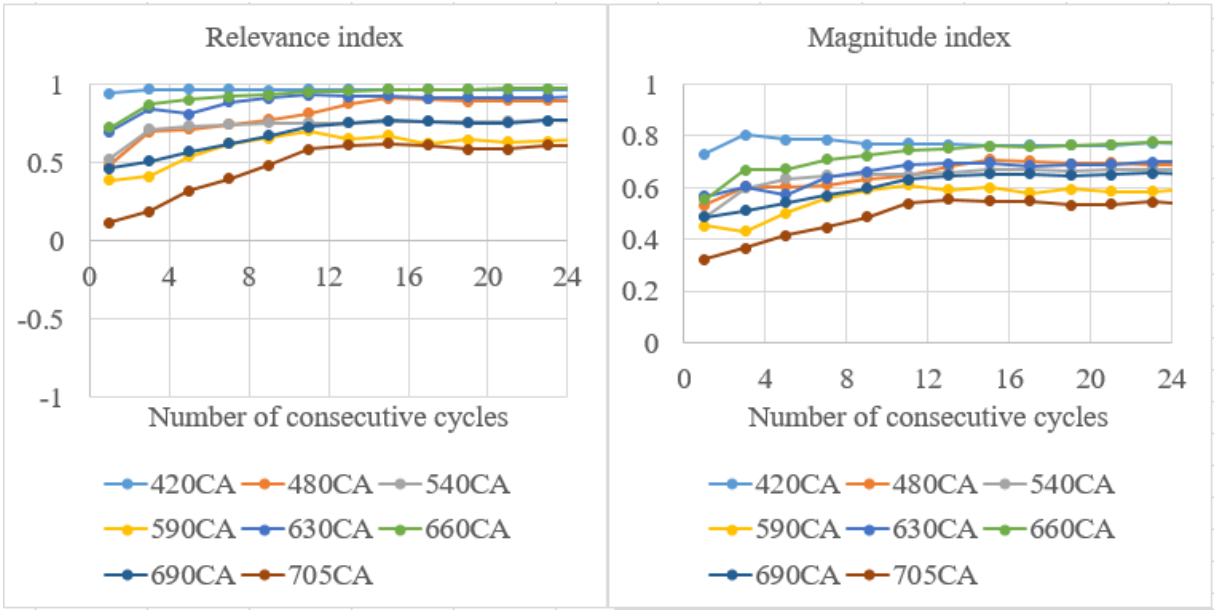

Figure 7. Evolution of RI and MI spark plane correspondence metrics at different points of the cycle in the DDES computation of the previous project.

Based on the results of Figure 9-Figure 11, it is clear that the correspondence between the CFD and the PIV is not decreasing from OP B to OP A and OP C, in contrast to what one could expect from the increase in Reynolds number. This result may be attributed to the following factors:

- The flow over valves in OP B is highly pulsating and a lot of high-speed backflow is present, potentially causing higher sensitivity to phenomena such as phase errors during the intake process
- Improvements resulting from the refined GT-Power models in the newer computations
- Impact of the turbulence model. In contrast to wall-modelled LES, the scale-resolving DDES approach (similar to [15]) was previously adopted in OP B due to its stabilising effect during the intense valve overlap period of OP B. However, it is possible that the DDES formulation leads to suboptimal (grey area, see e.g. [16]) regions during the intake/compression processes. An additional DDES simulation of OP C is carried out to directly compare DDES and WMLES.

It is noted that the performance of the DDES model is inferior to the WMLES in the late stages of the process. Hence, the improvements from OP B can at least partially be attributed to this factor. For DDES, similar result correspondence is observed between OPs B and C; where for the former, the results are better during compression.

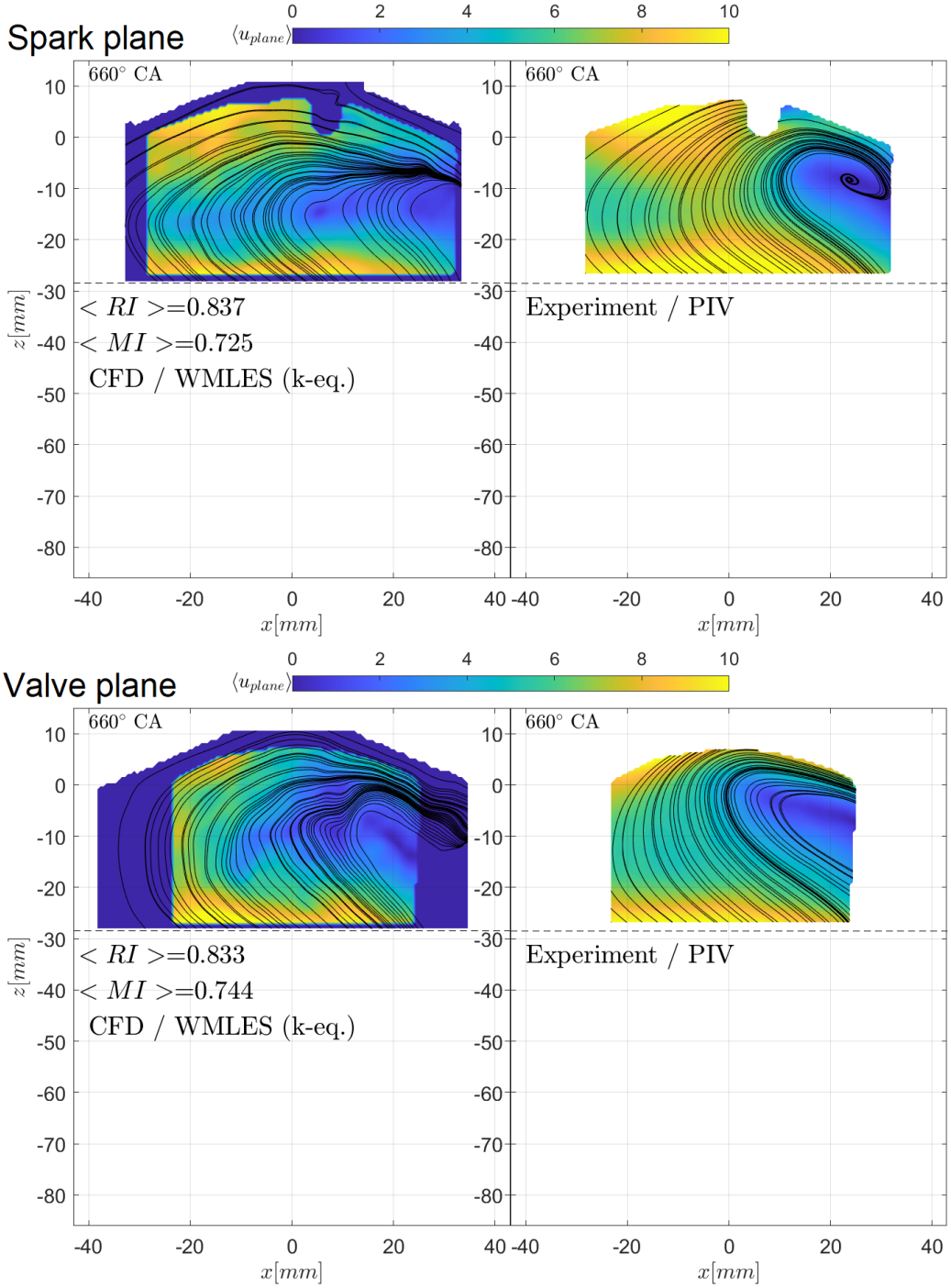

Figure 8.Spark plane (top) and valve plane (bottom) velocity field comparison between CFD and PIV, as well as mean relevance and magnitude index means at 660 CAD during compression. OP C with 0.75 mm grid.

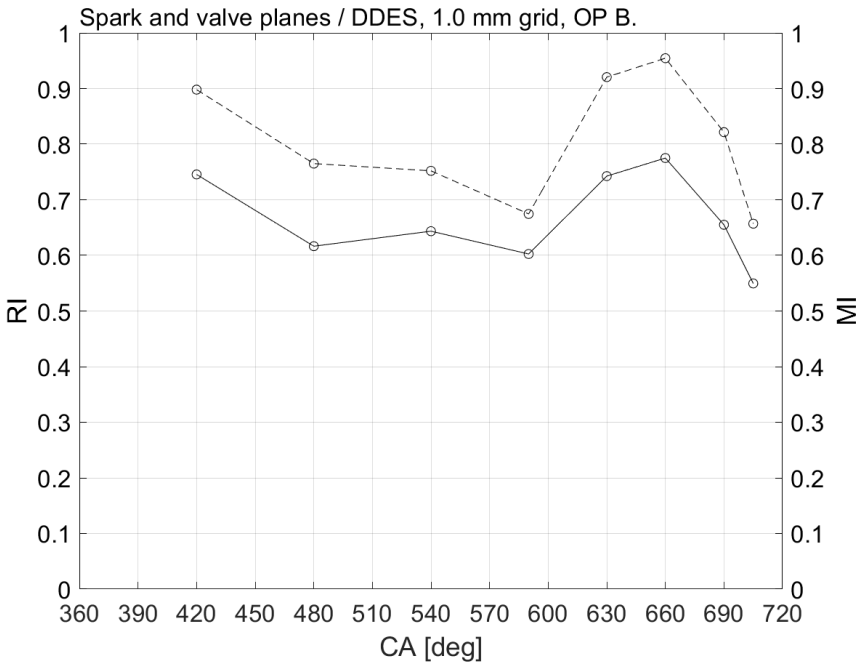

Figure 9. Mean relevance (dashed) and magnitude (solid line) indices between PIV and DDES (previous project) in the spark plane. OP B, 1.0 mm grid.

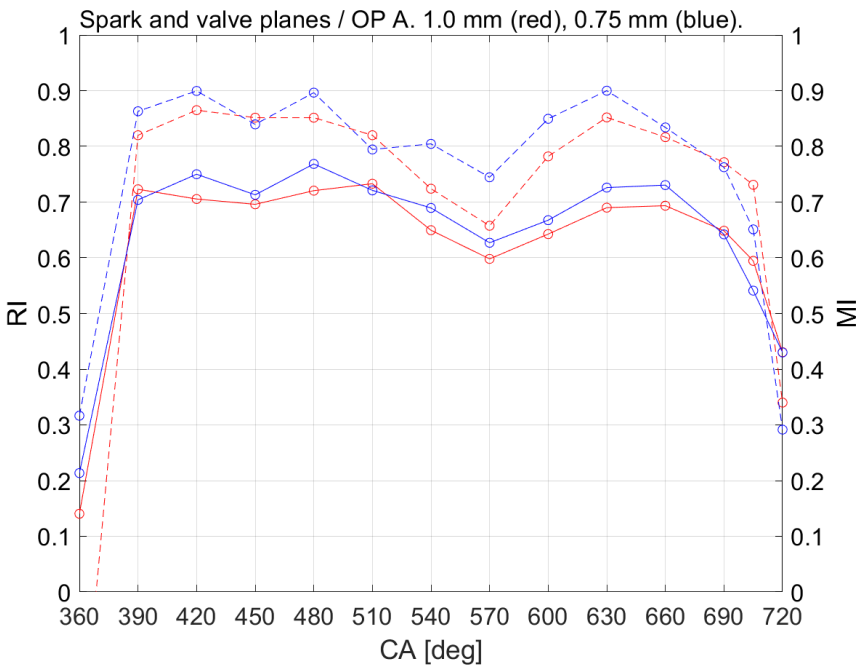

Figure 10. Collated WMLES result correspondence in multi-cycle simulation of OP A, against PIV measurements. 1.0 mm resolution (red), 0.75 mm (blue). Relevance and magnitude indices are denoted with dashed and solid lines, respectively.

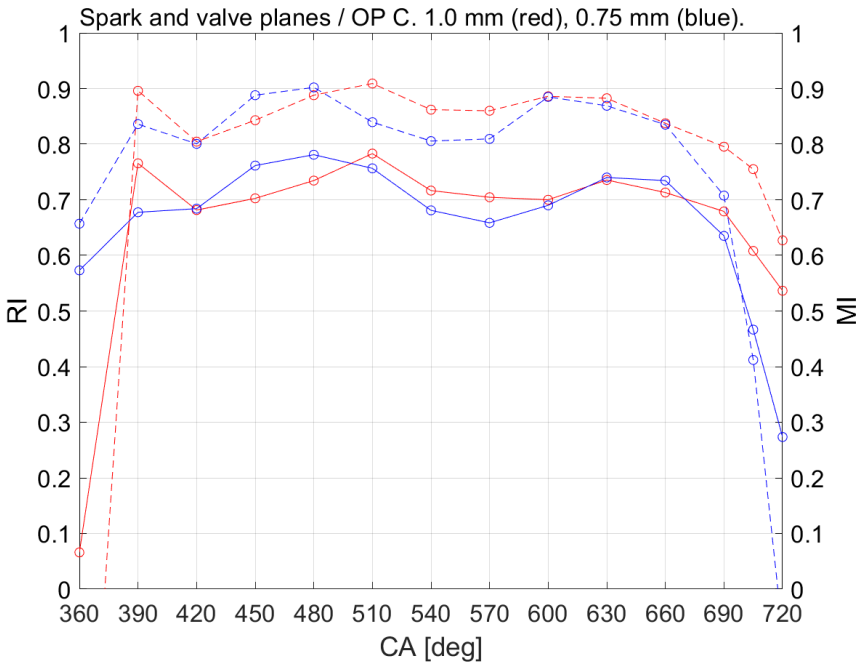

Figure 11. Collated WMLES result correspondence in multi-cycle simulation of OP C, against PIV measurements. 1.0 mm resolution (red), 0.75 mm (blue). Relevance and magnitude indices are denoted with dashed and solid lines, respectively.

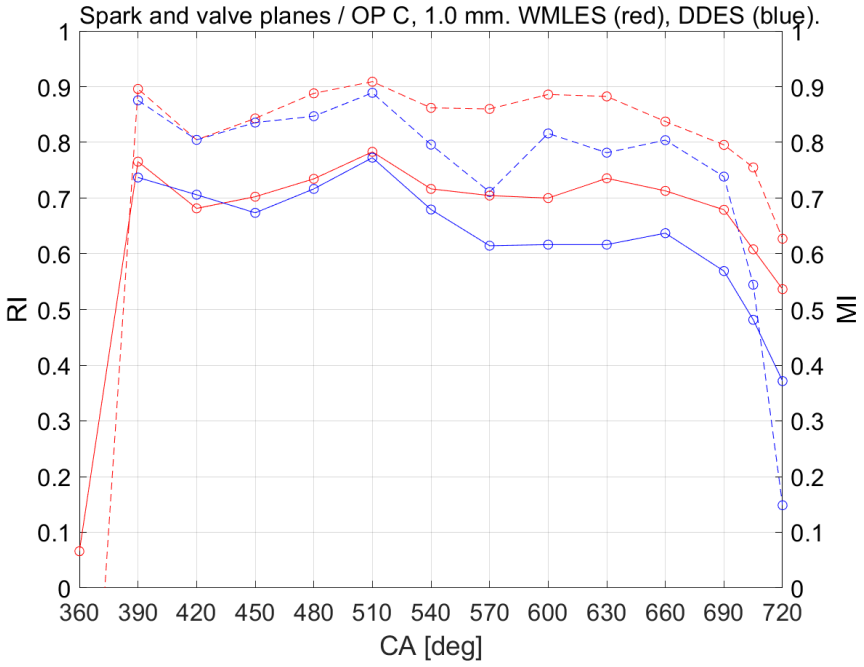

Figure 12. Collated result correspondence in multi-cycle simulation of OP C, against PIV measurements. WMLES (red), DDES (blue) with 1.0 mm grid. Relevance and magnitude indices are denoted with dashed and solid lines, respectively.

It is furthermore notable that between OPs A and C (with similar modelling approaches but a ca. 2-fold difference in Reynolds number), quantitative differences in mean flow experimental correspondence are minor. This is a promising indication for the representativeness of the multi-cycle simulation for OP E at a significantly higher engine speed.

3.2.2 LES resolution metrics at the new operating condition (OP E)

Resolved and modelled contributions of the simulated flow field fluctuations are important metrics for the quality of large eddy simulations. Although different such metrics have been proposed [17], there is no clear consensus in the literature regarding an optimal metric. Here, we employ the simple modelled-to-molecular viscosity ratio μ_{sgs}/μ, in which 0 would represent a DNS and increasing values refer to higher modelled contributions. The effect of increasing resolution on the instantaneous flow field and SGS metric is shown in Figure 12 exemplarily at 450 CAD where the piston speed attains its maximum value. The reduction of the modelled contribution as the grid is refined can be clearly seen.

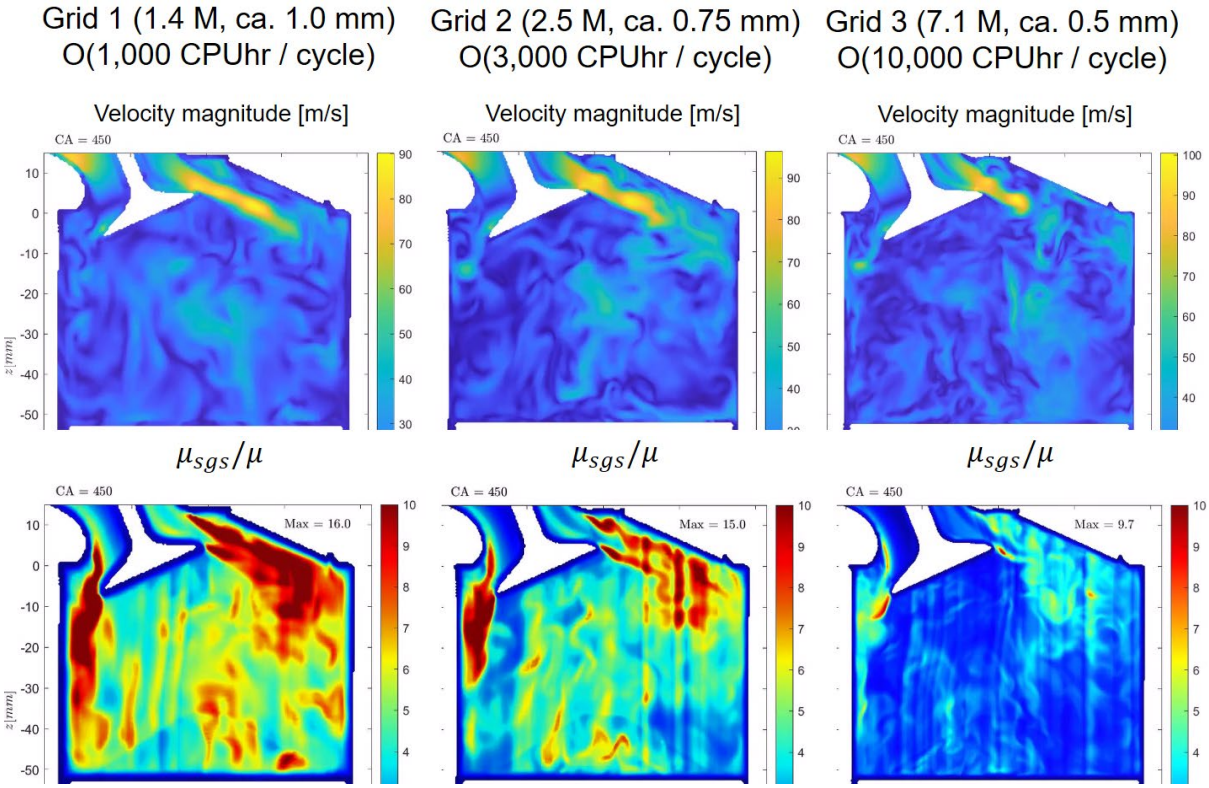

Figure 13. Velocity (top) and scaled SGS viscosity (bottom) snapshots with standard (left), intermediate (centre) and fine (right) resolution. The timing is at mid-compression (close to maximal piston speed) at 450 CA.

The examination of the modelled viscosity close to the end of compression (Figure 14) shows another interesting detail. Corresponding with the intake, one generally expects that larger grid sizes (and hence, filter sizes) contribute to larger values of the SGS viscosity. In Figure 14, such a trend is clearly absent between Grid 1 and Grid 2, indicating that the coarsest grid cannot sufficiently resolve the breakdown into small-scale turbulence. Thus, for late-stage processes at OP E, it is not meaningful to make detailed observations using Grid 1.

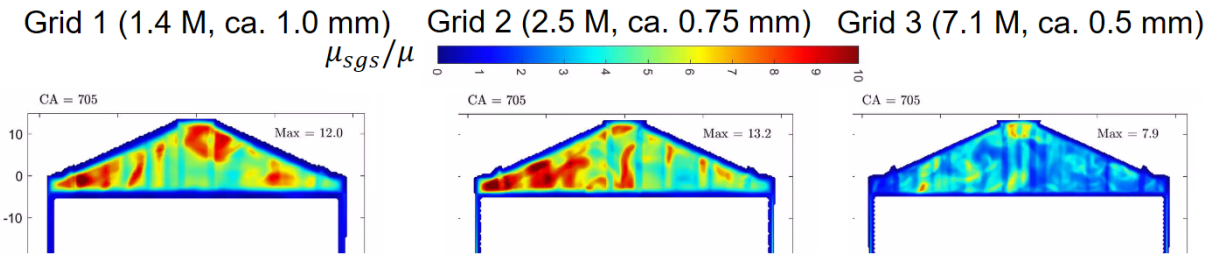

Figure 14. Modelled-to-molecular viscosity ratio contours close to the end of compression with standard (left), intermediate (centre) and fine (right) resolution.

3.2.3 The feasibility of a high-resolution wall-resolved LES of OP E

OP E (2500 RPM / 0.95 bar intake pressure) is at a significantly higher Reynolds number than the operating point investigated in the previous project with LES and DNS. In order to successfully carry out a wall-resolved large-eddy simulation, two near-wall grid criteria need to be fulfilled:

- Scaled wall-normal resolution $y_1^+ \sim 1$
- Scaled wall-tangential resolution $\Delta x^+ \sim 20$

The goal is to estimate the viscous length scale (VLS) δ_μ on the wall surfaces at the new OPs in order to reach such criteria. Based on previous measurements, the VLS can be accessed at all measured operating conditions A-D and at different crank angles (660, 675, 690, 705 CAD). For canonical cases, for a constant density flow one would assume that the shear velocity scales as

$$u_\tau \propto Re_D \tag{3}$$

where Re_D is a bulk Reynolds number. Equivalently, in variable density flows

$$\rho u_\tau \propto Re_D \tag{4}$$

The viscous length scale is defined as

$$\delta_\mu = \frac{\mu}{\rho u_\tau} = \frac{\nu}{u_\tau} \tag{5}$$

In the absence of strong variation in molecular viscosity (i.e. of the wall temperature), the viscous length scale should be related to the bulk Reynolds number as

$$\delta_\mu \propto 1/Re_D \tag{6}$$

Here, we consider the characteristic Reynolds number of the engine operating point to scale as $\mathrm{Re} \sim p_{int} \cdot \mathrm{RPM}$. In Figure 15, the resulting VLS estimates with different colours denote different CADs. In correspondence with the previous relationship, a fit in the form of $\delta_\mu = \mathrm{A}/\mathrm{Re_D} + \mathrm{B}$ is suggested, where A > 0 and B >=0 are tuned for each CAD. The VLS at the highest Reynolds number (corresponding to 0.95/2500) can be estimated from this fit, and is displayed in Figure 15 (left).

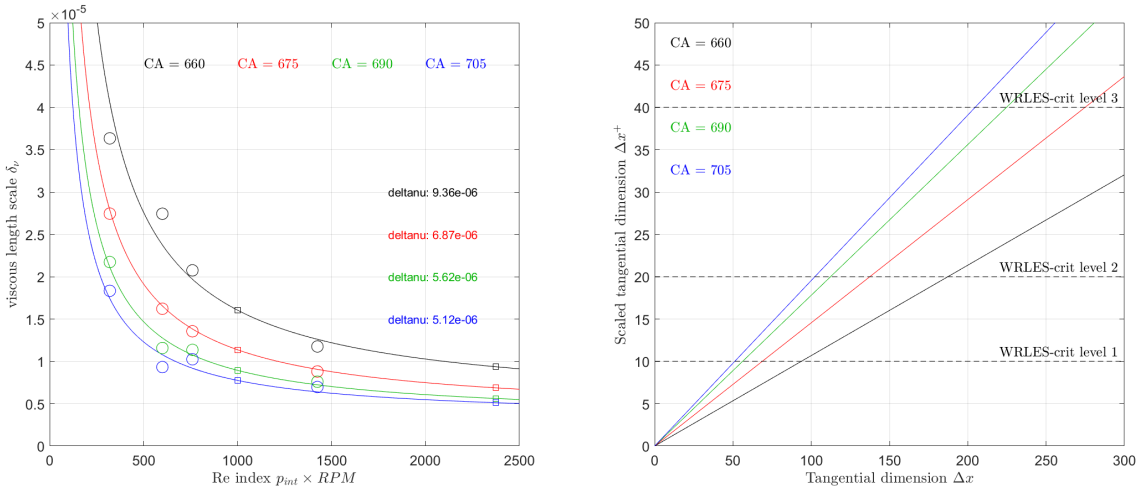

Figure 15. Determination of viscous length scale estimates for the new operating conditions (left). Scaled tangential spacing projection for a WRLES as a function of the dimensional tangential dimension, at different times of the compression stroke (right).

The rightmost final markers in the plot represent the points of interest: the estimated VLSs for OP E. Using the estimate, the maximal wall-normal resolution for the wall-adjacent point is ca. 5 microns. The projection for Δx^+ as a function of the physical spacing follows. Considering the relatively strict criteria set for WRLES such as $\Delta x^+ < 20$ (in the range of literature requirements, see e.g. [18]) it would appear that wall-tangential dimensions of ca. 0.1 mm are required and was employed in the present high-fidelity WRLES.

3.2.4 Code benchmarking: Star-CD vs Simcenter CCM+ (OP C)

As a means of cross-validation, we compare the Star-CD/es-ice platform to the recent Simcenter CCM+ code (also licensed by Siemens). The codes are based on a considerably different meshing approach. The Star-CD/es-ice platform (Figure 16, left) employs layers of cells which are continuously removed as meshing progresses. In contrast, the Simcenter CCM+ mesh (Figure 16, right) is based on a Cartesian, equidistant grid with local refinements and a separate prism layer grid close to the wall. The transition to this near-wall grid is then made via adaptive cells. The specific points of interest include

- Does either code appear to be decisively superior in terms of mean flow correspondence?
- Are there specific phases of the engine process that appear to be better replicated with one code?
- How does code performance change (improve) with increasing resolution?

Computations were carried out over at least 10 cycles for all code/grid combinations. This is usually a sufficient number for the convergence of mean flow RI and MI metrics.

Figure 17 compares Star-CD/es-ice (left), PIV (centre) and Simcenter CCM+ (right) phase-averaged velocity fields at time instances during the intake (450 CAD) and compression (660 CAD). It is evident that the major characteristics and large-scale vortices are well captured by both codes. In terms of quantitative metrics, the Star-CD solution is more accurate during intake, while the CCM+ solution is more accurate during compression. Although the displayed images are from single points in time, this is a more widespread trend.

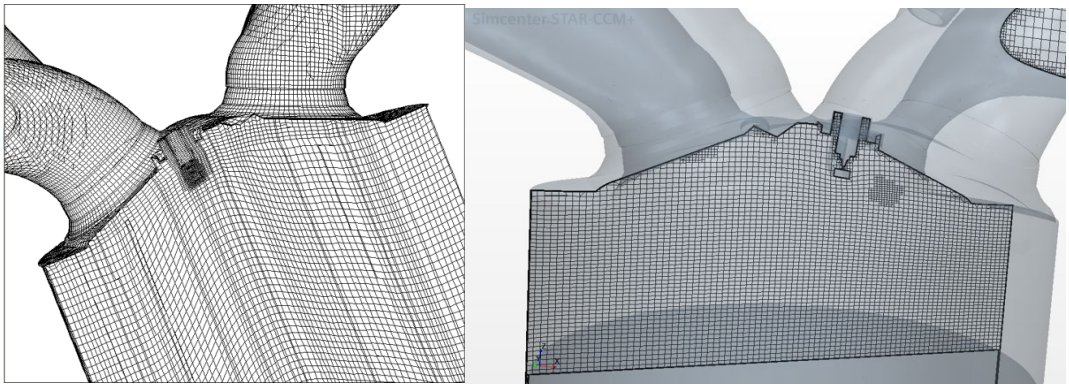

Figure 16. Examples of grids constructed by Star-CD / es-ice (left) and by Simcenter CCM+ (right)

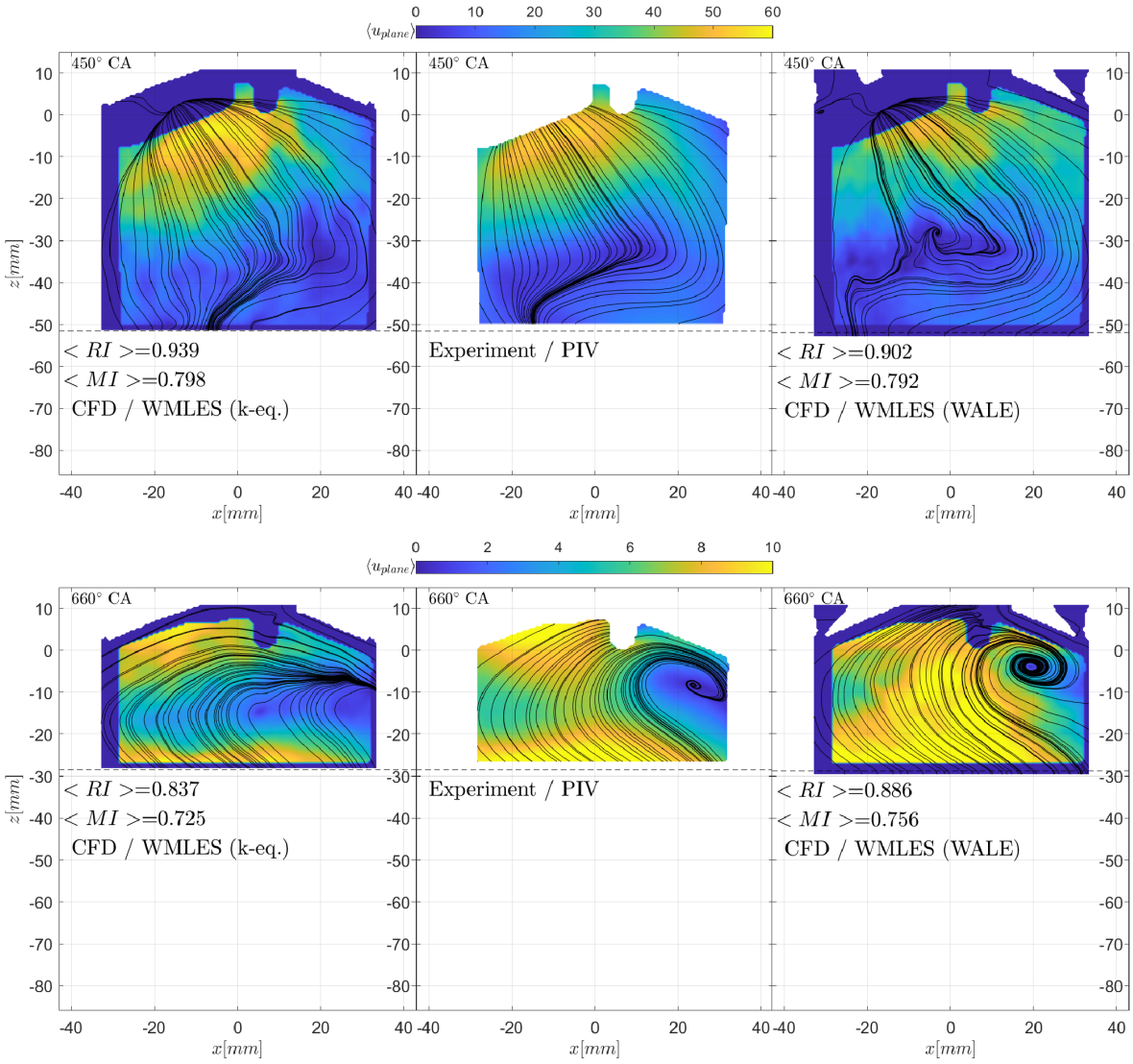

Figure 17. Comparison of spark-plane phase-averaged velocity fields between Star-CD (left), PIV (centre) and Simcenter CCM+ (right). Intake (top, 450 CA) and compression (bottom, 660 CA) processes.

To elaborate on this statement, Figure 18 displays a collated view of the average MI and RI metrics throughout the cycle. It is clearly notable that RI and MI values are higher for Star-CD during the intake process, and lower during compression. The computation in the CCM+ code appears to maintain a stronger tumble vortex, which may contribute to the better correspondence during compression. Figure 18 also shows improvements with increasing computational resolution. For Star-CD, there is a noticeable increase in mean flow fidelity with resolution, particularly during compression. For CCM+, the change from 1.0 to 0.75 mm bulk resolution results in a smaller improvement, focussing mainly on the intake stroke.

To summarise, the performance in terms of collated mean flow fidelity appears to be similar between both codes, using similar mesh resolutions and identical boundary conditions. However, significant phase-specific differences exist. Importantly, the present results indicates that the Star-CD/es-ice package yields performance in line with that of a recent, state-of-the-art code such as Simcenter CCM+.

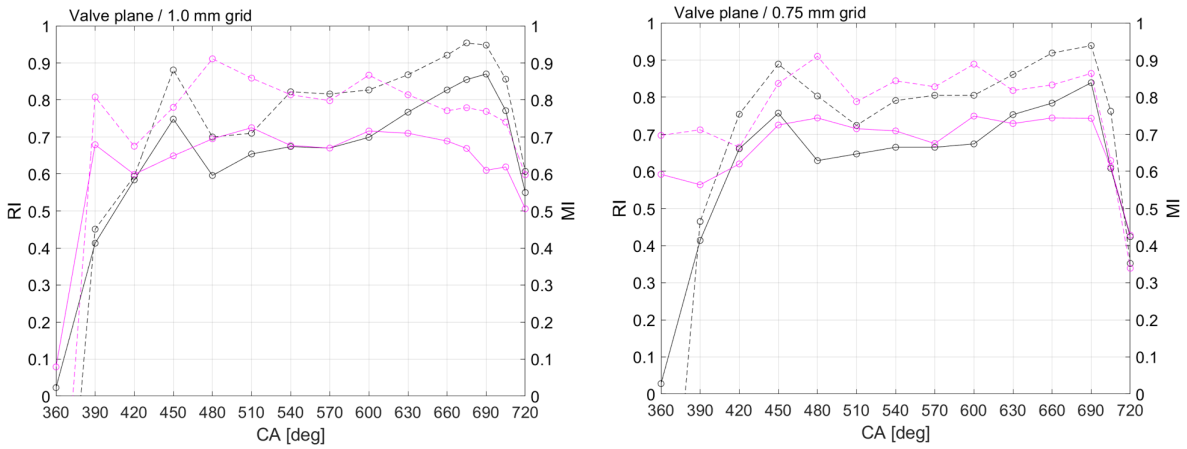

Figure 18. WMLES at engine OP C (1500 RPM / 0.95 bar). Collated comparison of mean flow fidelity between Star-CD (magenta) and Simcenter CCM+ (black) throughout the intake and compression strokes. 360 degrees denotes TDC at the beginning of intake. Relevance and magnitude indices are denoted with dashed and solid lines, respectively.

3.3 Non-reactive simulations at the new operating point

3.3.1 Multi-cycle WMLES for OP E: Star-CD vs Experiment

Figure 19 shows an example of the correspondence between CFD and PIV in the 0.75 mm case, while Figure 20 displays a collated set of RI and MI values for different bulk resolutions (1.0 and 0.75 mm). The correspondence between the WMLES and PIV is excellent in the present case, and superior to the lower RPM OP A and C. Such a result is counterintuitive as it is expected that, given similar spatial resolution, higher Reynolds numbers lead to higher modelled contributions and error of the flow solution. The higher correspondence may, among other reasons, be due to (a) lower sensitivity to boundary conditions (such as accurate valve motion) and (b) better WMLES wall model applicability. Regardless, it appears that SGS contribution is not a dominant factor in terms of mean flow correspondence in the present cases.

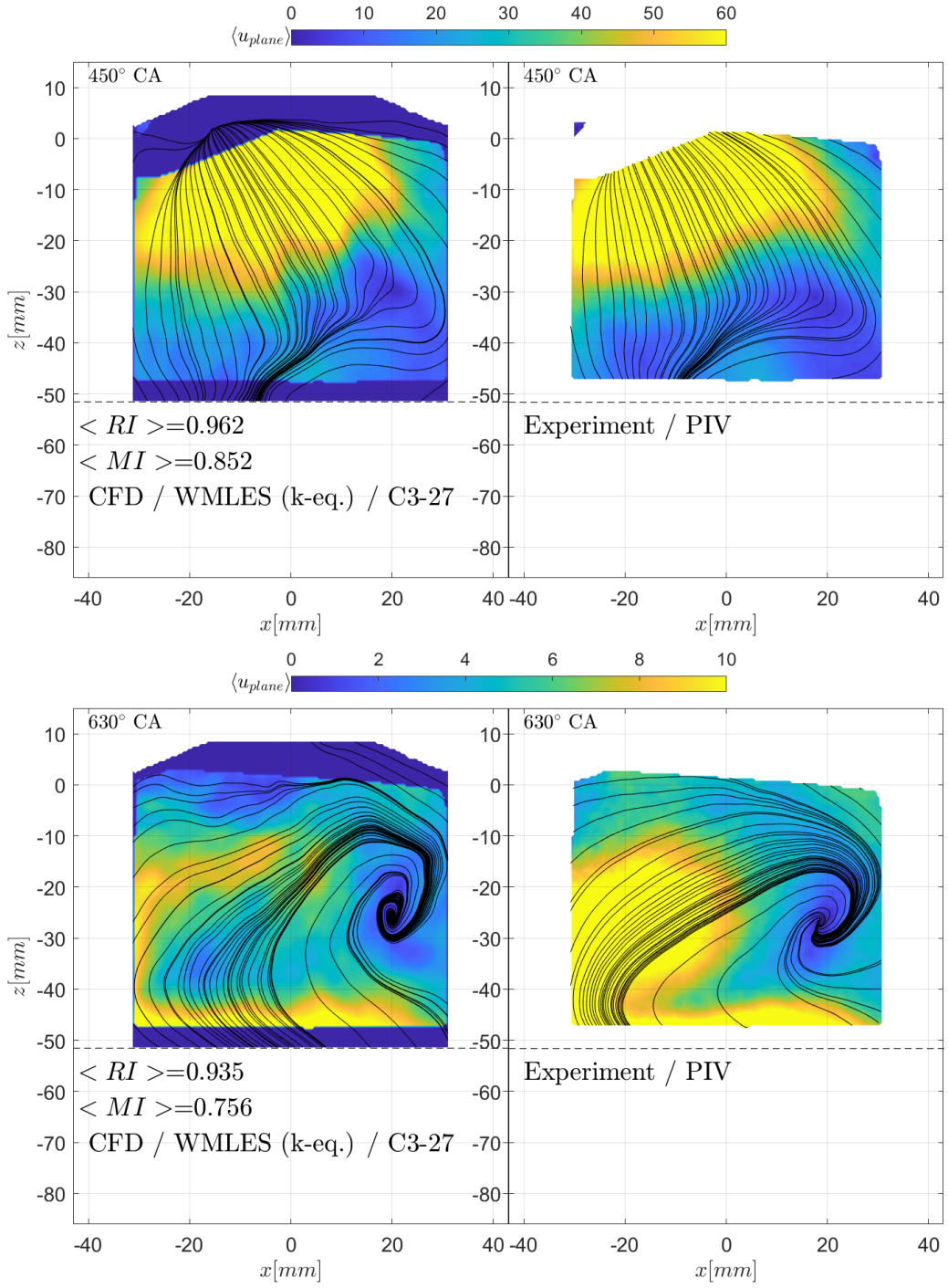

Figure 19. OP E (2500 RPM / 0.95 bar). Planar phase-averaged velocity fields in WMLES (left, over 25 cycles) and PIV (right). Mid-intake (top) and mid-compression (bottom) phases.

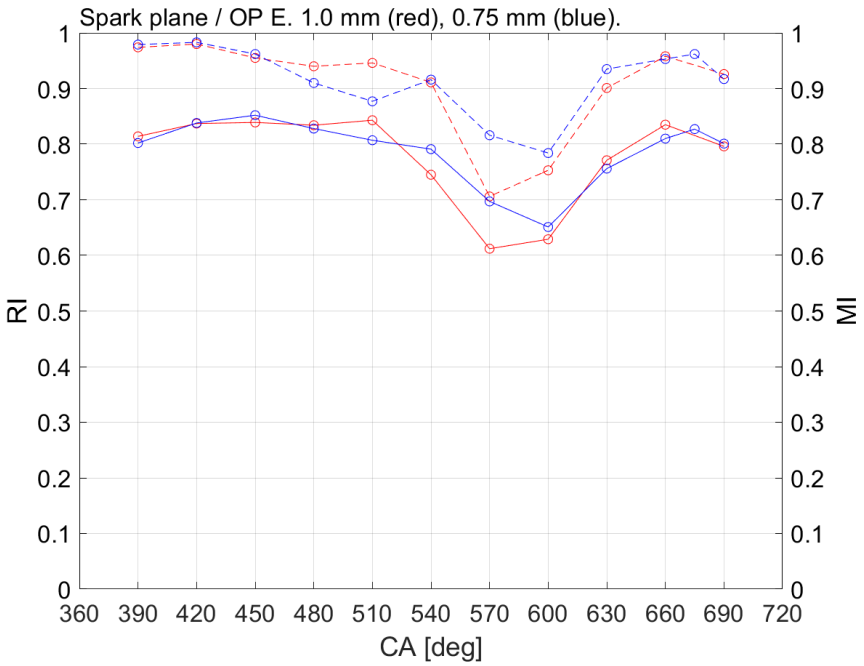

Figure 20 Collated result correspondence in multi-cycle WMLES simulation of OP E. 1.0 mm grid (red), 0.75 mm grid (blue). Relevance and magnitude indices are denoted with dashed and solid lines, respectively.

3.3.2 Towards the high-resolution wall-resolved LES in OP E

For the completion of wall-resolved LES at OP E, a multi-cycle computation was performed in line with the workflow strategy of OttoWallHeatXfer. Boundary conditions were adopted from the data in Figure 6. At the time of this simulation, no experimental data were available for reference, so quantitative comparisons were not possible. Regardless, the prospect of carrying out the high-resolution simulation, which was not part of the original project plan, provided valuable and reliable results for comparison with WMLES.

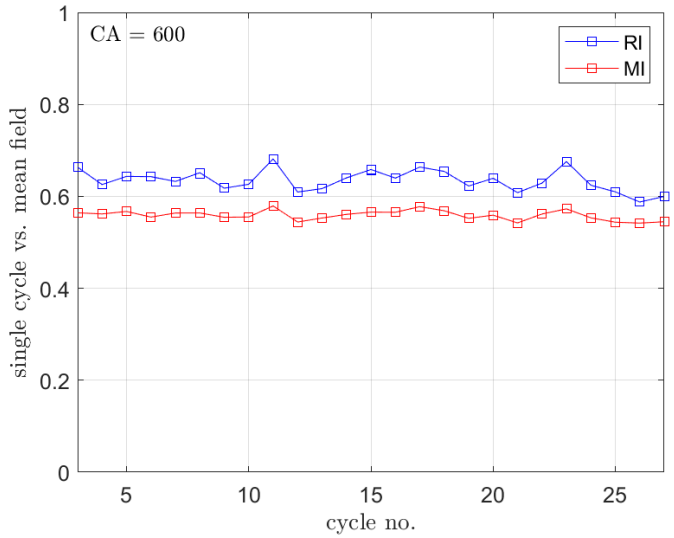

Figure 21. Correspondence between each individual cycle (between 3-27) and the mean cycle in terms of RI and MI in the multi-cycle WMLES.

In order to select the cycle that most closely resembles the mean cycle, the relevance and magnitude indices were computed in three dimensions over all cells in the domain, between individual cycles and the mean cycle (Figure 21). As a result, cycle 11 was selected for the high-resolution computation.

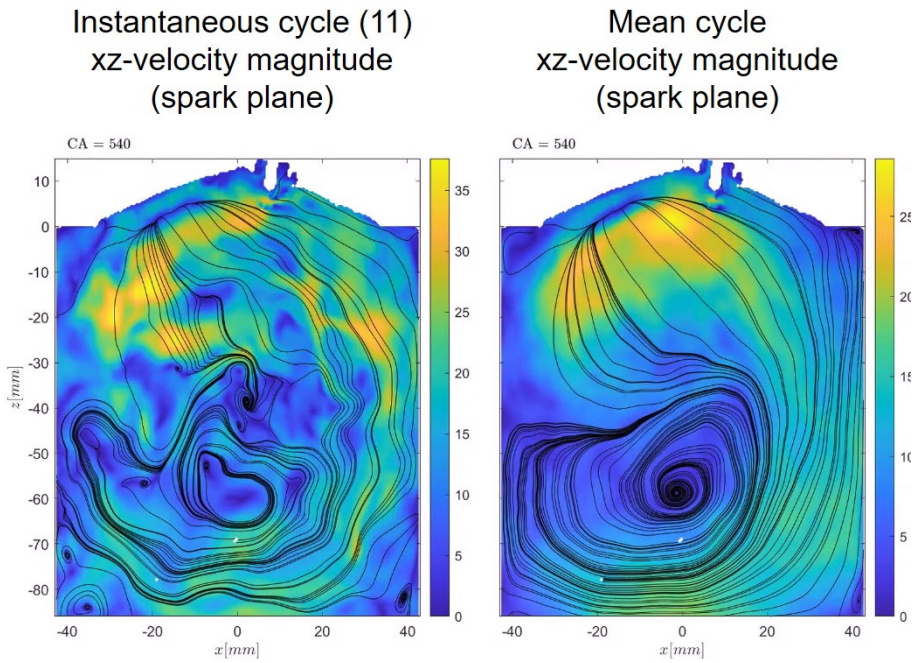

Figure 22. Vertical plane velocity field, OP E. Instantaneous (left) and mean (right) cycles.

The intake stroke and early compression was computed using the fine Grid 3 (Figure 13). The result was mapped onto the high-resolution grid akin to the DNS mapping that was carried out in the previous project for OP B.

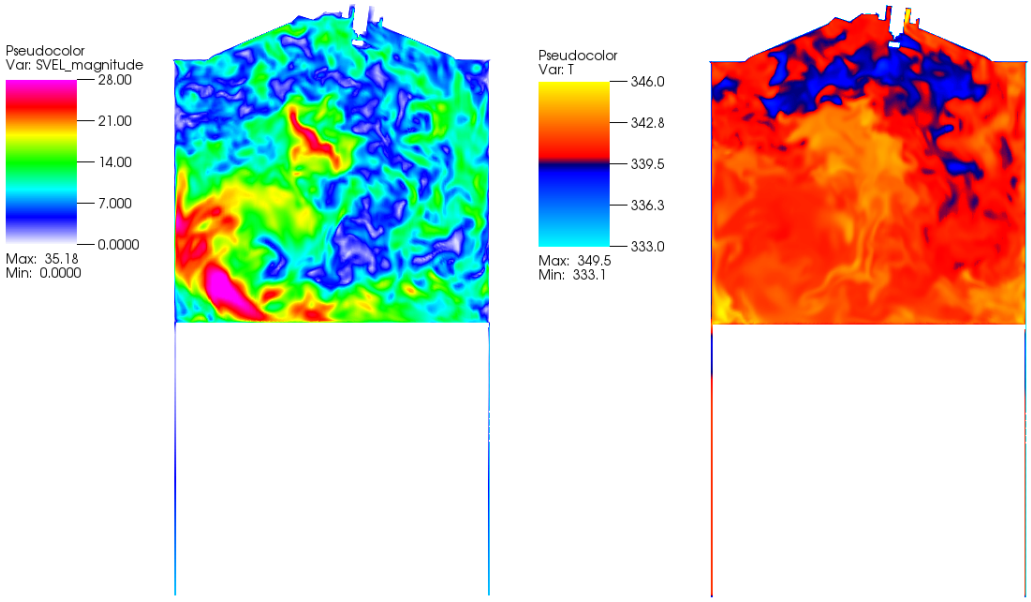

Figure 23. Initial condition for the high-resolution wall-resolved LES at 600 CA. Velocity magnitude (left) and temperature (right).

3.4 Wall-resolved LES of the OP E compression stroke

3.4.1 Model setup

The model setup for the WRLES computation follows the DNS workflow established in OttoWallHeatXfer. The methodology of the solver requires a conforming hexahedral grid, a precondition that renders mesh generation highly non-trivial. In-house algorithms have been developed and used in combination with Trelis [19] for the generation of computational grids that accurately captures the complex geometric features of the engine while fulfilling the necessary mesh restrictions and quality criteria. The grids were constructed by filling the cylinder head volume with tetrahedral elements (TETs), and subsequently converting each TET to four hexahedrons (HEXs).

In order to generate the initial condition, a methodology to map the flow and temperature fields (Figure 23) from LES onto the highly-resolved WRLES grid was developed. This enables the initialization of the compression stroke of the DNS with data obtained from the LES, and allows for the direct comparison of selected cycle between LES and DNS. An efficient mapping algorithm based on the VTK library [20] is employed.

Figure 24 displays the (*a posteriori*, i.e. formed after completing the computation) dimensionless metrics for different grids on the piston surface. The scaled grid sizes are defined as $y^+ = \rho u_\tau y/\mu$ and $x^+ = \rho u_\tau x/\mu$ where material properties are defined at the wall temperature. As expected, the conditions and grid metrics become stricter towards the end of compression.

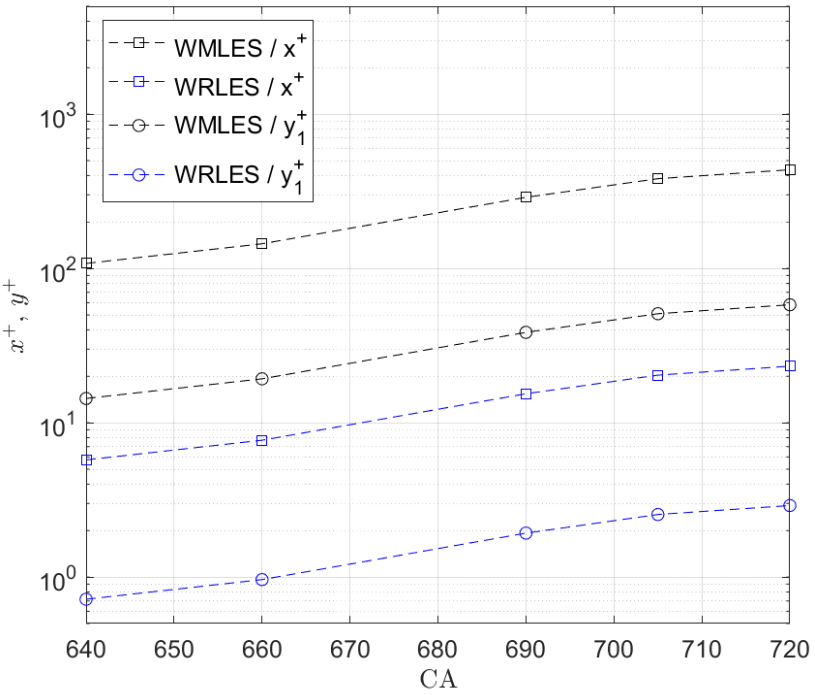

Figure 24. Non-dimensional grid metrics on the piston surface for WMLES (0.75 mm grid) and WRLES

3.4.2 Qualitative observations between OP B and OP E

As noted in Figure 25, the primary difference between the high-resolution computations of OP B (previous project) and the new OP E is the velocity and thermal length scales. The vertical structures are far smaller in OP E, and the temperature field displays better mixing. In the thermal near-wall region, qualitatively similar plumes of cold gases are inclining in both cases. Again, the length scales of these plumes

are smaller in the WRLES of OP E. It is notable that, as in the initial condition from WMLES, the large-scale flow patterns are similar. This concerns particularly the accelerating tumble flow that impinges on the piston -- the wall jet flows along the piston surface and is then directed first toward the cylinder liner and subsequently towards the spark plug.

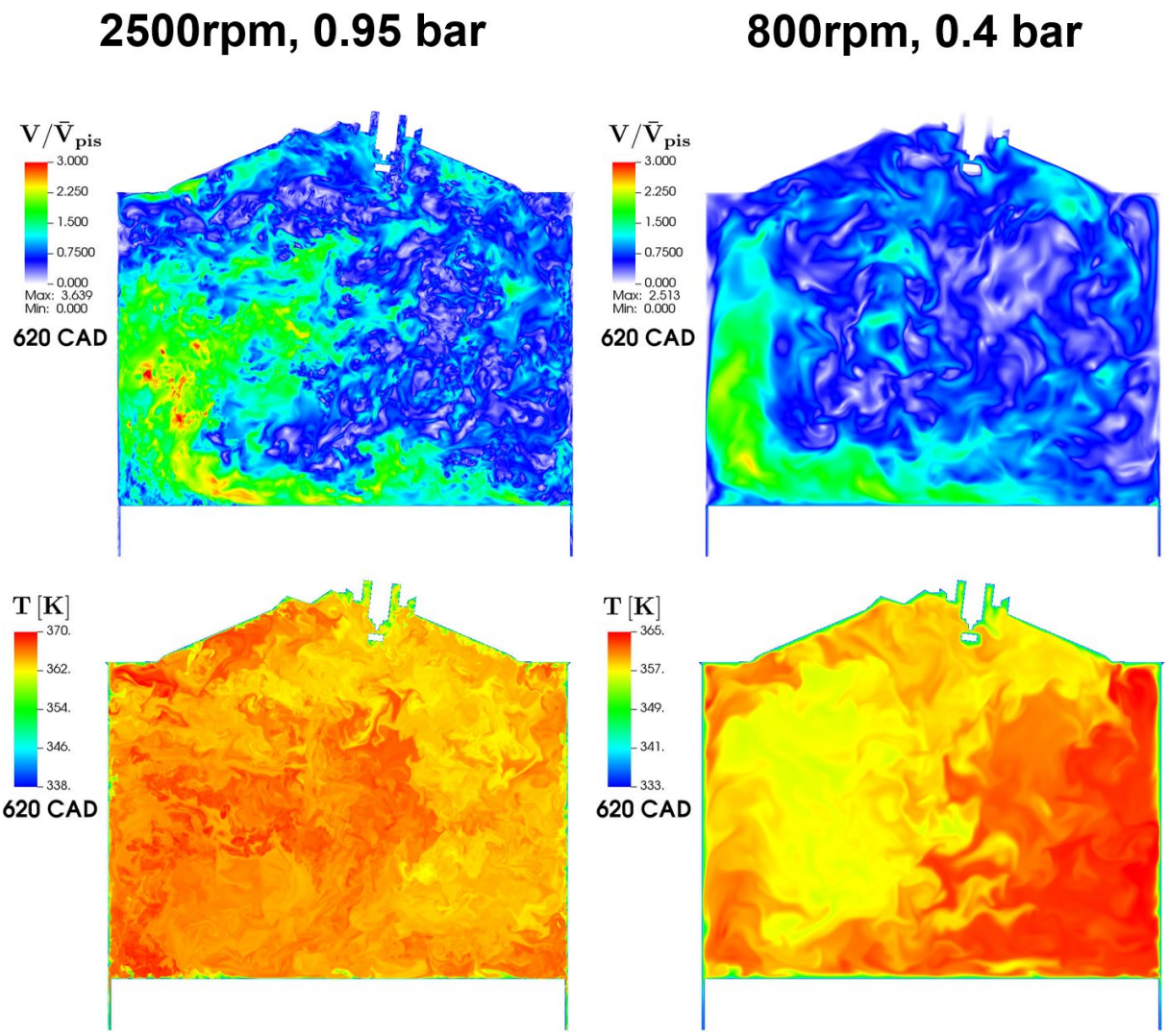

Figure 25. Instantaneous velocity (top) and temperature (bottom) fields in the WRLES of OP E (left), and in the DNS of OP B (right), at 620 CA, shortly after initialisation from WMLES data.

At later times (Figure 26 and Figure 27) the coherent tumble motion has partially broken down. Still, the tumble signature is visible on the piston surface and close to the cylinder head. While thermal mixing has already advanced to a rather homogeneous state in Figure 25, the considerable impact of wall heat transfer on the thermal fields is visible at later stages. This observation is consistent with the previous work of Schmitt et al. [21] in an engine-like geometry. Both velocity and thermal fields are likely subject to significant variation close to ignition timing, although the former is likely to be more significant [22-24].

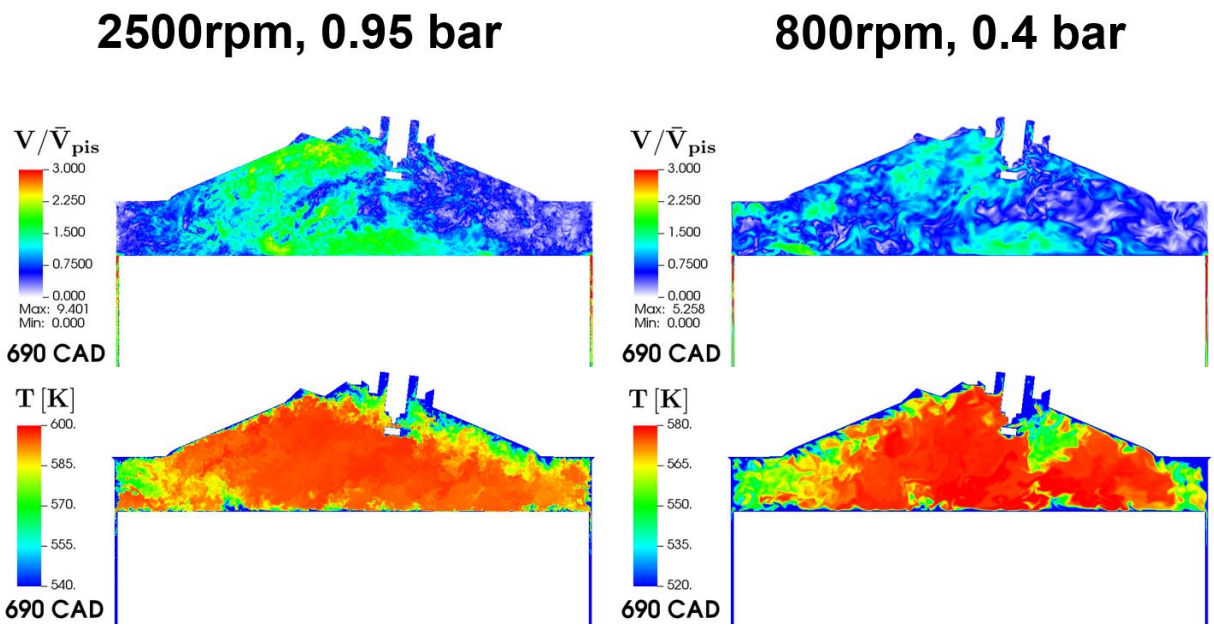

Figure 26. Instantaneous velocity (top) and temperature (bottom) fields in the WRLES of OP E (left), and in the DNS of OP B (right), at 690 CA.

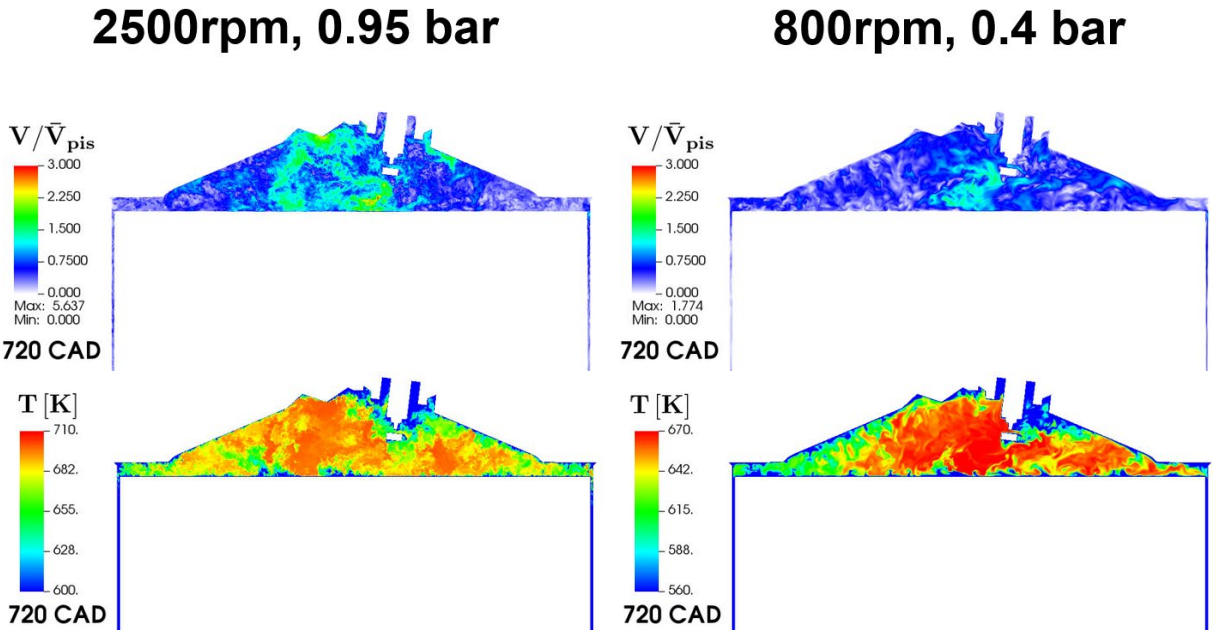

Figure 27. Instantaneous velocity (top) and temperature (bottom) fields in the WRLES of OP E (left), and in the DNS of OP B (right), at 705 CA.

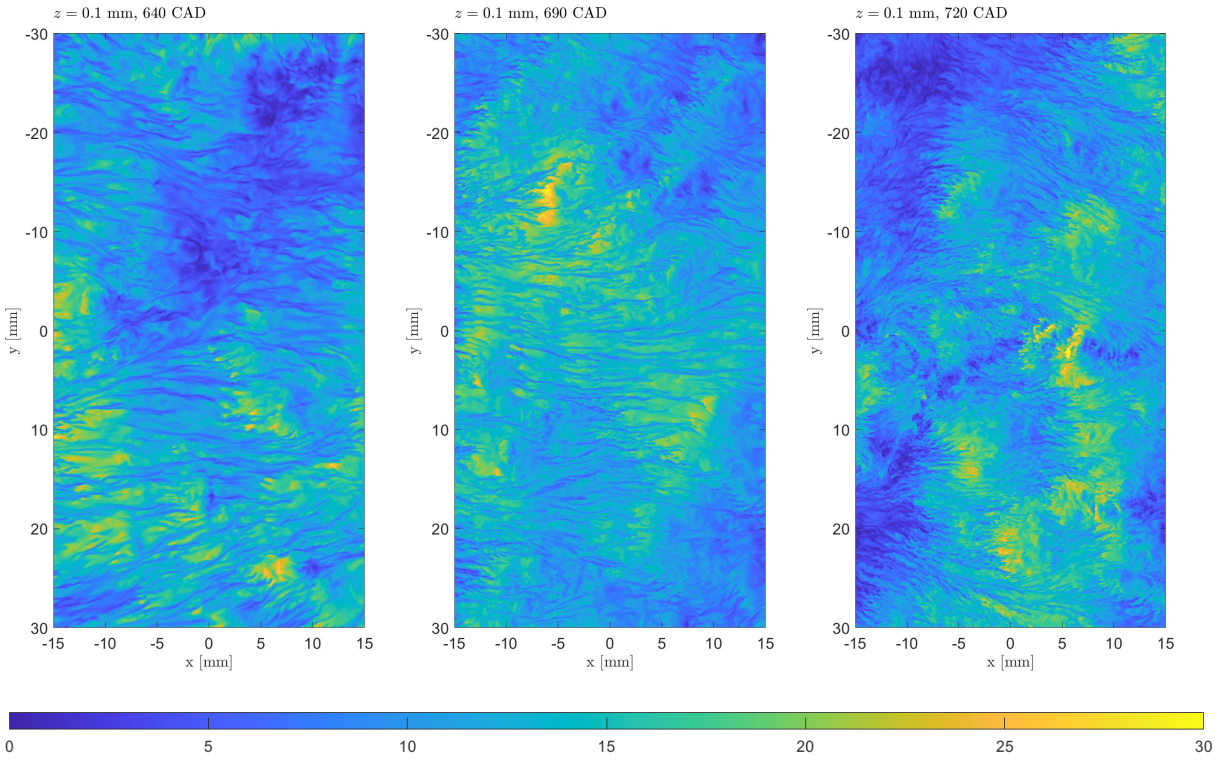

Figure 28. Instantaneous velocity magnitude fields in the WRLES simulation of OP E in a rectangular region at a distance of 0.1 mm from the piston surface, at 640, 690, and 720 CAD.

Instantaneous velocity fields close to the piston surface are displayed in Figure 28. The same trend of reducing flow scales can be noted here as well. Moreover, the streaks at the latest time instance (TDC) are far less uniformly oriented, indicative of the flow topology change due to vortex breakdown close to TDC.

3.4.3 Near-wall boundary layer profiles: change from OP B to OP E

In our previous work [8], the deviation of the scaled boundary layer profiles from “ideal laws” was established for OP B. These results, captured in the piston surface vicinity, together with new results from the WRLES of OP E, are shown in Figure 29. It is noted that at the higher load and engine speed of the new OP, the profiles also deviate from the ideal behaviour. This time, however, the deviations are different, and the boundary layers profiles are much better developed. The boundary layer is significantly thicker (in dimensionless units) and the profiles are shifted to higher values, characteristic of a more developed state. Such a trend has also been previously observed experimentally between OPs B and C [25]. The thermal boundary layers also display a similar trend (Figure 28, right column). In summary, it can be stated that engine boundary layers do not appear to follow ideal behaviour in OP E, but the global applicability of standard models appears to be better in comparison with OP B.

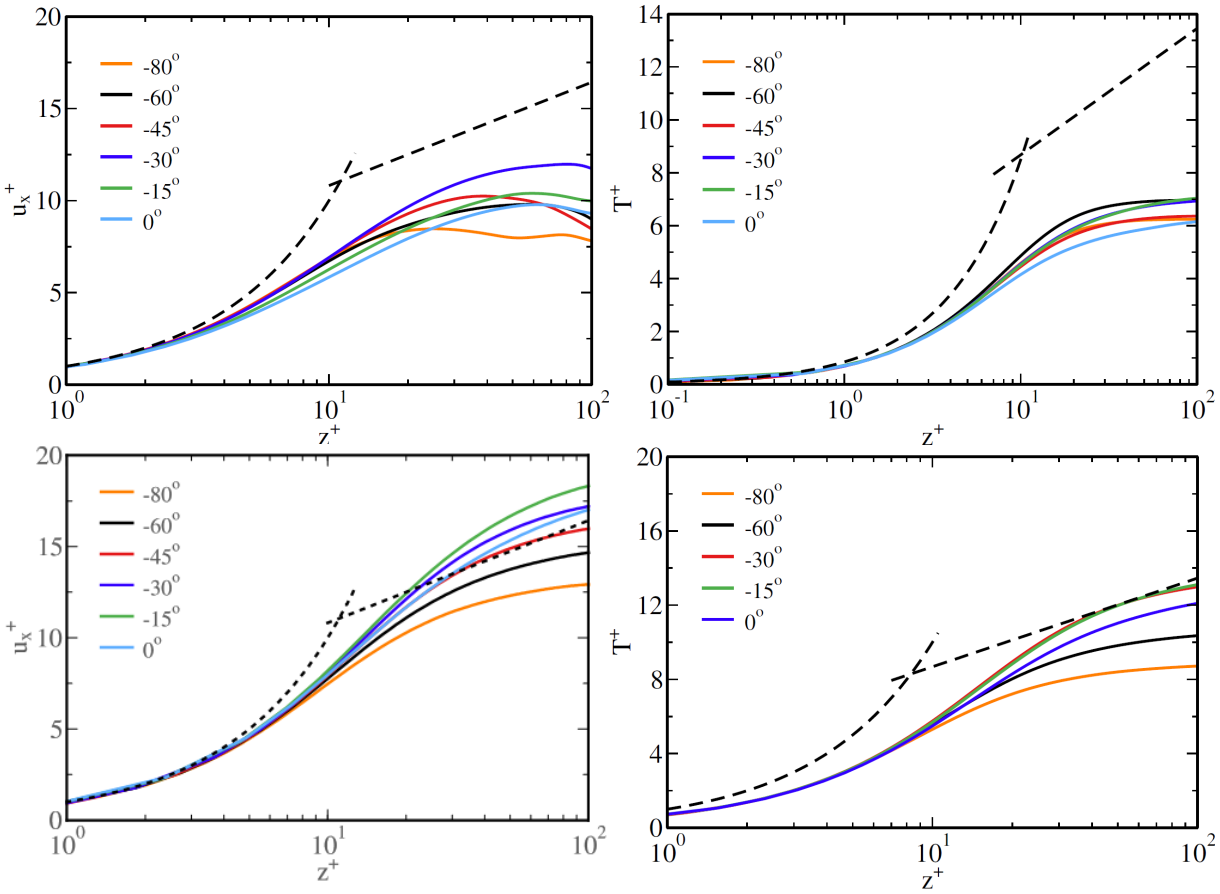

Figure 29. Top: DNS of OP B (previous project), bottom: WRLES of OP E (present project): Scaled momentum (left) and thermal (right) boundary layer profiles. Adshed lines denote the linear-log-law.

3.4.4 Locality of near-wall boundary layer scaling

The profiles shown in Section 3.4.3 were obtained from a rectangular region corresponding with Figure 28, spanning a surface of 30 60 mm (for reference, the engine bore is 86 mm) around the centre of the piston surface. In this region, the flow is significantly impacted by the tumble motion, and there is a dominant flow direction. The box size sensitivity was investigated (not shown here), and differences between 20 x 40 mm and 30 x 60 mm were low. While such data adoption provides a good overall impression of the scaled profiles, the flow structure varies in the combustion chamber. To demonstrate this, we divide the box region into three distinct subdomains (Figure 30). The flow generally advances from region 3 to 2 to 1. The corresponding boundary layer profiles are shown in Figure 31. We revisit first the DNS results of OP B from the previous project [1, 2].

Comparing Figure 30 and Figure 31, distinct trends in the boundary layer velocity profiles can be discerned. This is particularly prevalent at later times (690 and 705 CAD): as the boundary layer develops (from right to left), the scaled boundary layer profiles shift upward in the graphs (starting from green, in stripe 1). The profiles drawn beneath the dashed ideal flow lines are indicative of regions where the flow has not developed fully, such as those seen in the near-field of impinging jets [26]. This characteristic is further demonstrated by displaying the mean stream-wise pressure gradient in the plots: a positive (adverse) pressure gradient denotes a blockage, while a negative pressure gradient signifies wall jet development. At 705 CAD, the red curve even indicates partial flow separation, which can be acknowledged by comparing with the bottom frame of Figure 30.

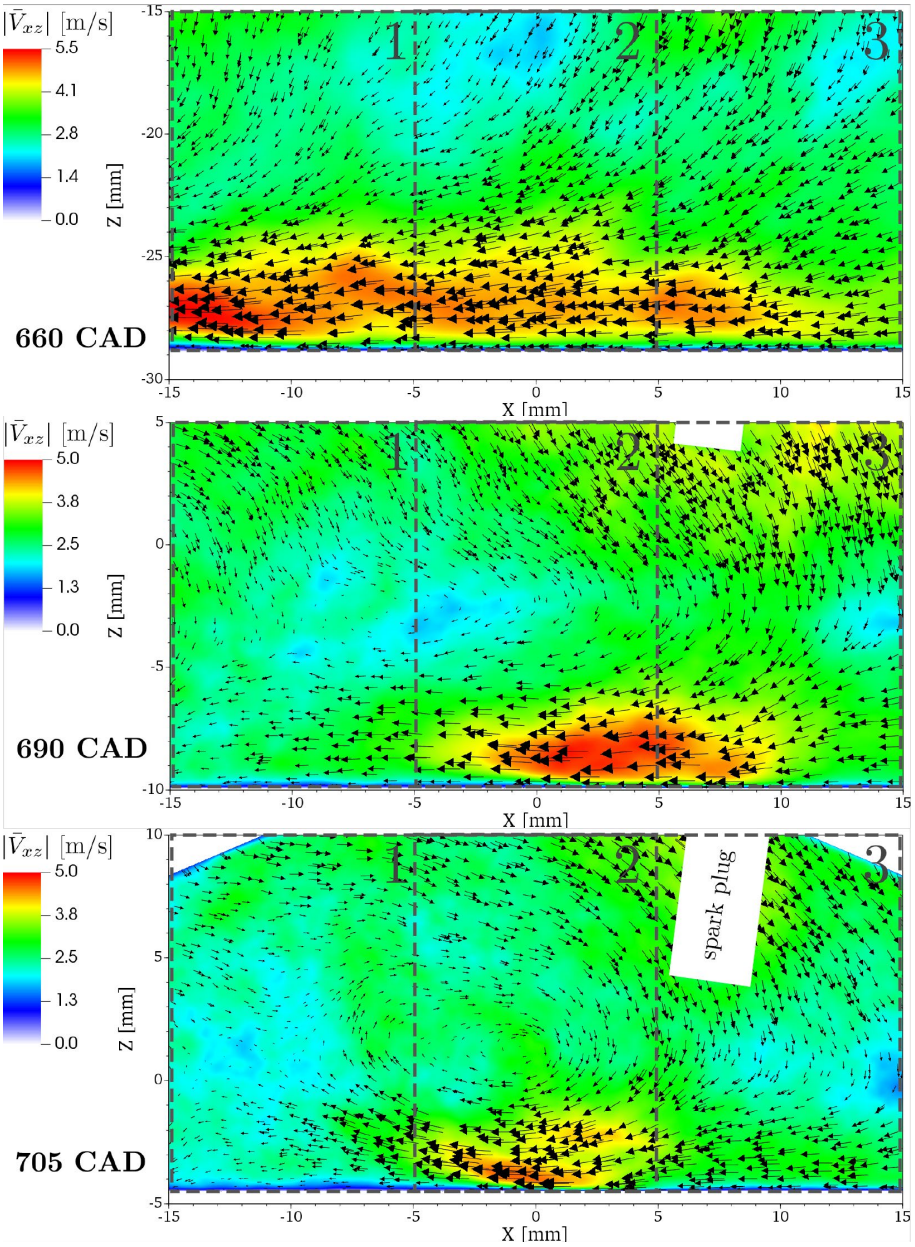

Figure 30. Spanwise-averaged mean flow fields during compression of the DNS in OP B.

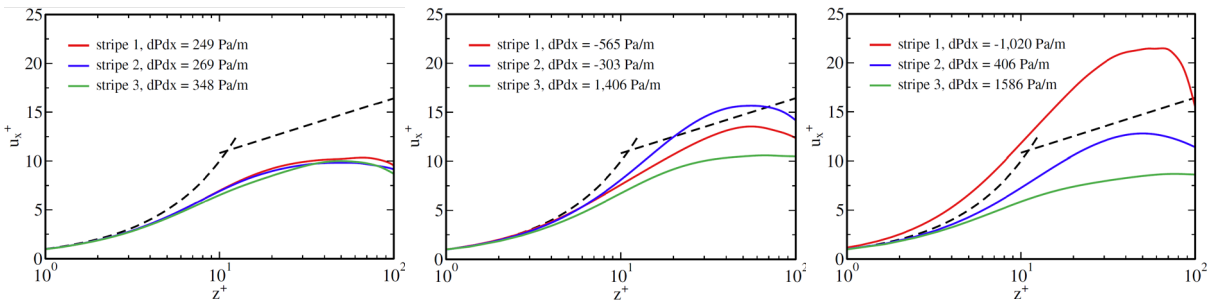

Figure 31. Velocity boundary layer profiles at different sub-regions of the near-wall piston region, from the DNS of OP B. at 660 (left), 690 (centre), and 705 CAD (right).

This analysis emphasises the strong spatial variation of the velocity boundary layers. In general, for the low RPM operating condition, the flow is not highly developed following impingement, leading to the deviation of the boundary layer profiles from ideal behaviour, and the relatively poor applicability of typical wall stress models, resulting in underprediction of wall stresses.

It is then also interesting to investigate whether similar phenomena can be noted in the WRLES of the newly investigated OP E (Figure 32). Qualitatively, the tumble motion develops similarly: flow enters from the top-right corner, impinges on the piston surface, and develops into a wall jet, denoted by the region of high velocity above the piston surface. Compared with Figure 30. the flow fields are however not entirely similar: the near-wall flow appears to be aligned with the surface for a longer distance before changing its direction away from the piston and towards the cylinder head.

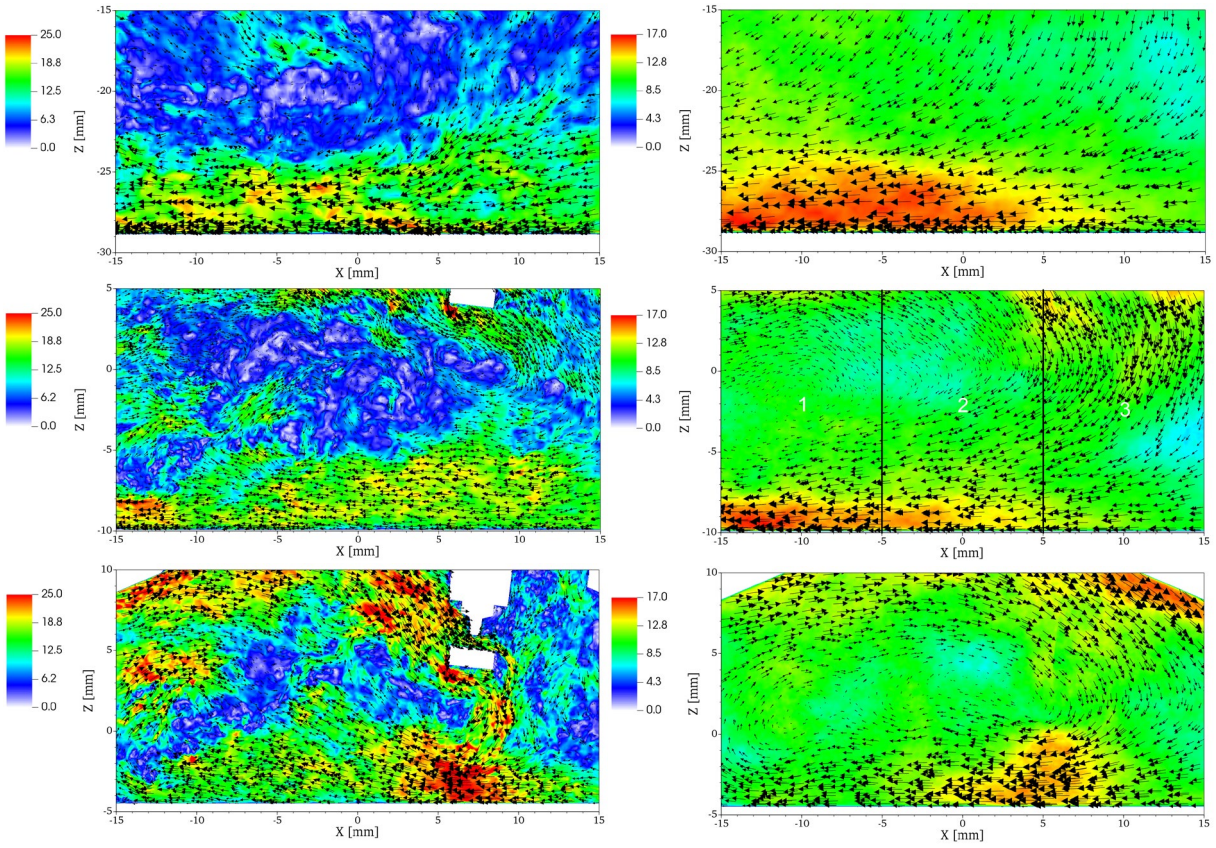

Figure 32. Instantaneous velocity magnitude distribution in the spark plane (left) and spanwise-averaged velocities (right), from the WRLES of OP E, at 660 (top), 690 (centre), and 705 CA (bottom).

The corresponding near-wall profiles are shown in Figure 33, and can be compared with the corresponding profiles of Figure 31. Overall, a similar trend is noted, with scaled profiles deviating from the logarithmic behaviour, and varying in space. The direction of the evolution is also similar to OP B, where the blockage-impacted Stripe 3 (with lower boundary layer development and high adverse pressure gradient) shows lower profiles with a considerable variation in time.

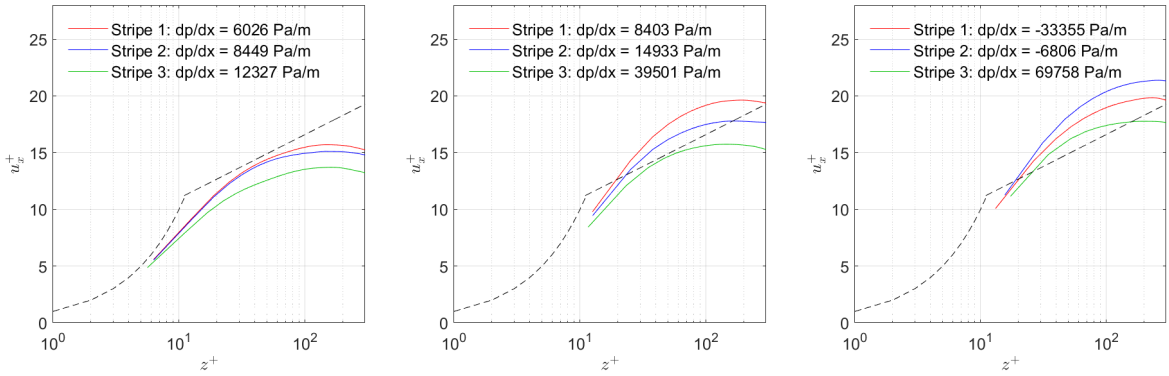

Figure 33. Near-wall non-dimensional momentum boundary layer profiles corresponding with Figure 32. Stripes 1-3 denote 10 mm regions from left to right. The mean streamwise pressure gradient for each region is also reported.

3.5 Wall model benchmarking

3.5.1 Model formulation

Two models are primarily tested here. The Plensgaard-Rutland (PR) model [4] is based on the Werner-Wengle power law for momentum and a modified Han-Reitz heat transfer model, was specifically developed for WMLES and yielded good results in a prior study [27] when compared with DNS of an engine-like flow, and is available in the Star-CD code. The algebraic model (ALG) [3] developed in the previous research project models the wall heat flux as

$$q_w = \lambda_w \cdot d\tilde{T}/dy\big|_W \cdot COEFF \tag{7}$$

where λ_w is the thermal conductivity at the wall temperature and $\tilde{T}$ is the filtered temperature at the wall-adjacent node. COEFF is a correction term (i.e. the wall model) which reads

$$COEFF = 1 + A[\Delta^+ \cdot \rho_w/\rho_2] \tag{8}$$

where A = 0.46 is a tuned model constant. The critical component of this model is the non-dimensional quantity Δ^+, an estimator of the ratio of grid spacing to thermal boundary layer thickness:

$$\Delta^+ = (\tilde{T}_1 - T_w)/(\tilde{T}_2 - \tilde{T}_1) \tag{9}$$

where subscripts 1 and 2 denote the first and second wall-adjacent cells, respectively. The model was implemented in the STAR-CD code via user subroutines for the purposes of this project.

3.5.2 TU Darmstadt Engine Case: motored OP B & motored OP E

Results of the wall model benchmarking are presented here both globally and in a component-specific sense. Figure 34 displays the breakdown of the combustion chamber components. It should be noted that as the piston moves upward, the area of the Liner decreases continuously, whereas the other components remain similar. Moreover, the Crevice walls notably include both the outer wall (part of the cylinder liner below the piston) as well as the inner wall (the piston skirt).

In the WMLES of OP E, the bulk (and wall-tangential) resolution is approximately 0.75 mm, while near-wall resolution varies between 0.1-0.2 mm. As shown in Figure 24, these lengths result in non-dimensional metrics of $y_1^+ = 20\text{-}140$ and $x^+ = 100\text{-}400$.

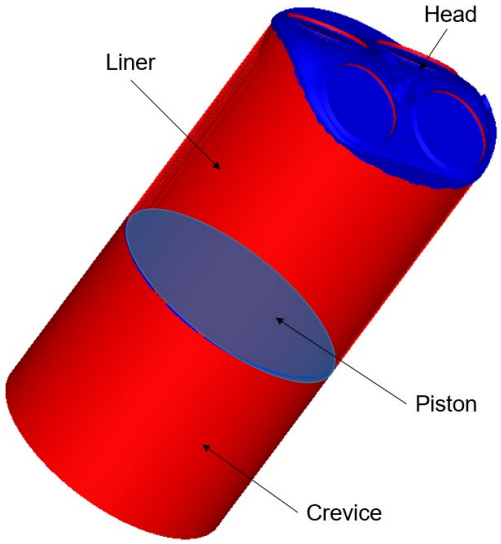

Figure 34. Components of the engine combustion chamber at BDC.

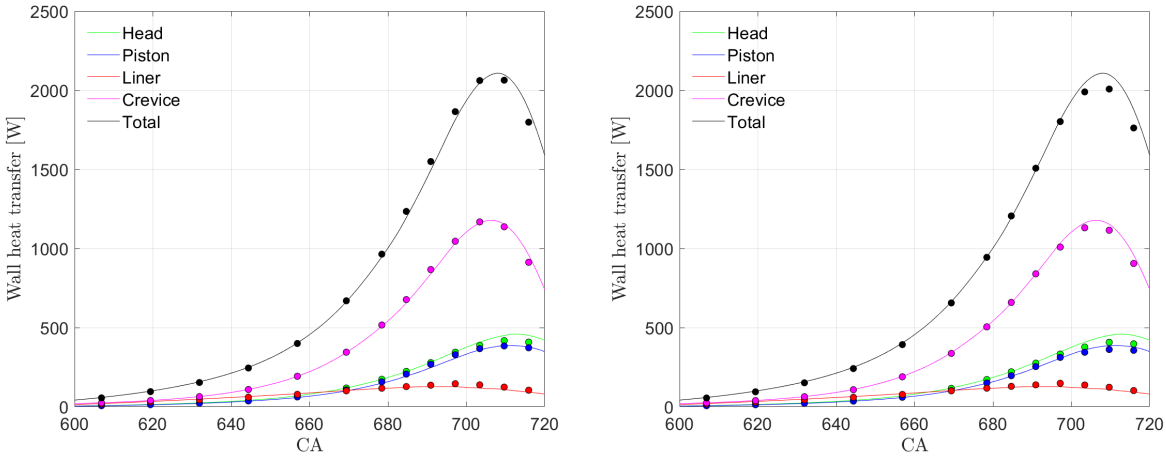

Figure 35. Global heat transfer over engine components in OP B with 1.0 mm grid. PR model (left), ALG model (right). DNS (solid lines), WMLES (filled markers).

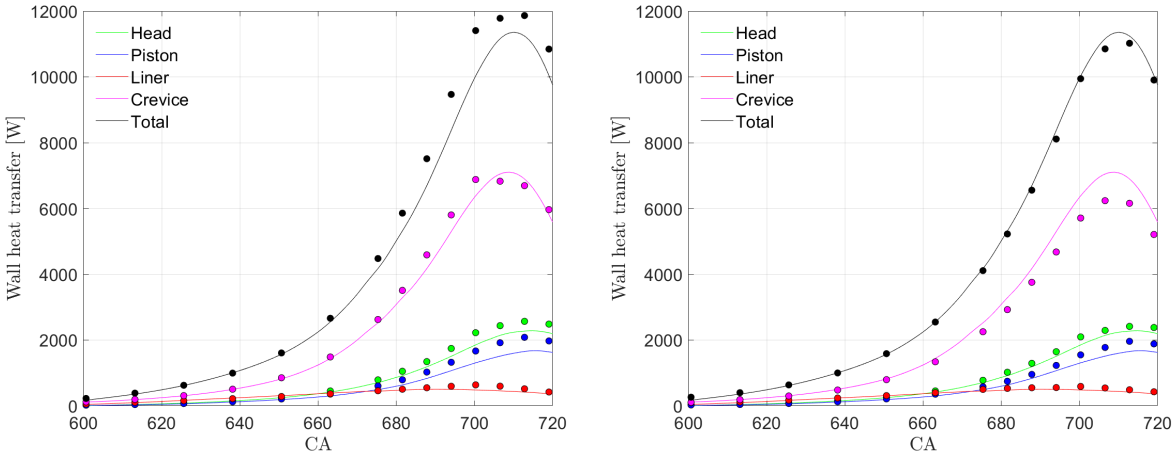

Figure 36. Global heat transfer during compression for different engine components for OP E, using the PR model (left), ALG model (right). WRLES (solid lines), WMLES (filled markers).

From Figure 35 and Figure 36 it is apparent that both PR and ALG models yield a reasonable reproduction of the DNS and WRLES global heat fluxes in OPs B and E, respectively. The total WHT prediction with the ALG model is consistent between OPs B and E, while the PR model mostly overpredicts HT in OP E. Here, let us recall that the PR model involves coupling between wall stresses and heat transfer, following the Reynolds analogy. In the past, the PR model was noted to provide good HT predictions even though wall stresses were substantially underpredicted [27] due to the real momentum scaling deviating significantly downward from the ideal line. With OP E, this scaling appears to be closer to the ideal line, being more suitable for the stress model. Concurrently, however, the HT prediction rises above the reference. In contrast, the ALG model is uncoupled from wall stress models.

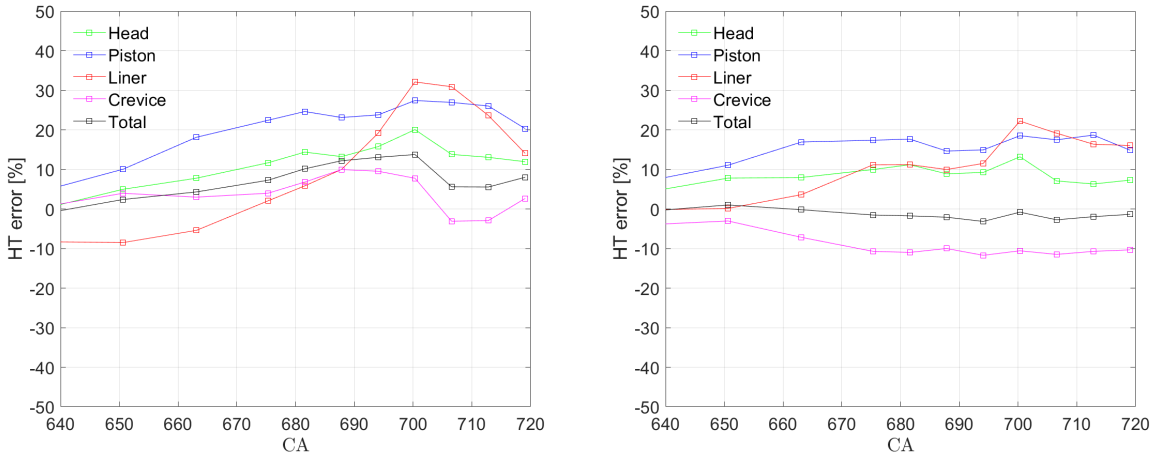

Figure 37. Componentwise mean heat flux prediction accuracy, OP E. PR model (left), ALG model (right)

As the exceptionally large crevice region is dominant in terms of the total heat transfer, it is instructive to investigate the componentwise relative HT difference in more detail (Figure 37). In general, slightly higher and more time-varying errors are noted in the PR model computation. The ALG model better reproduces the heat fluxes on the piston, head and liner, whereas the PR model performs better in the crevice region. It should be noted that in [3], the data-driven ALG model was trained without any data from the TUD engine (a priori validation was carried out against heat flux data on the piston, i.e. the blue curve in Figure 35). The present results serve as a strong indicator that the model has wider applicability

in WMLES and is not limited to its training operating conditions, or indeed the low Reynolds number of OP B.

For reference, the results in Figure 37 can be compared with standard Star-CD models (Spalding law for wall stress and log-law for heat flux) and a no-model approach (sometimes adopted due to low reliance on wall modelling, see e.g. [28, 29]). This comparison is shown in Figure 38, demonstrating that considerable errors are made when adopting such approaches with the present grid. It should however be noted that the standard model does not result in a catastrophic reduction in fidelity in comparison to e.g. the PR model, corresponding to the present WRLES indication that the more developed boundary layers are, on average, closer to the ideal flow behaviour.

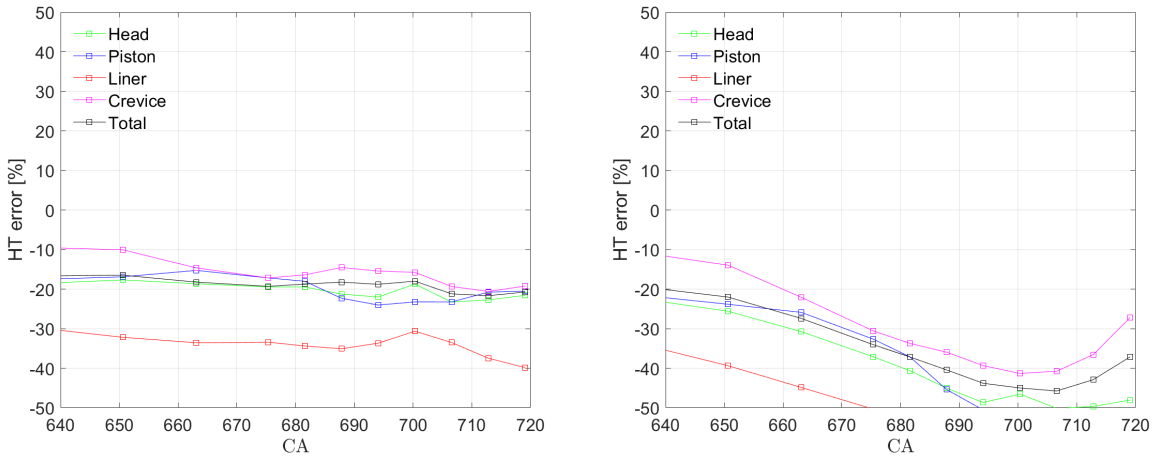

Figure 38. HT errors through the compression stroke in OP E, with the Star-CD standard approach (left) and a no-model appoach (right).

3.6 Explorative simulations in the fired OP E

A fired variant of OP E was generated in GT-Power and Star-CD to study potential differences in heat transfer prediction during reactive operation. The numerical configuration is as follows:

- Combustion model: G-equation level-set method [30]
- Spark ignition: energy deposit + Laminar-turbulent flame speed transition model [31] (spark timing: 32.8 CAD BTDC)
- Tabulated laminar flame speed as a function of pressure and temperature, based on the GRI 3.0 mechanism [32], accounting for 5% EGR. Flame speed tables were generated using Cantera.
- Damköhler model for turbulent flame speed with model constant (A = 9.0) adapted for LES
- Quenching model via a Wiebe-function, diminishing the total (sgs) flame speed towards the laminar flame speed in wall proximity
- Transient pressure/temperature boundary conditions at intake and exhaust manifolds from calibrated fired GT-Power simulations
- Wall temperatures estimated via private communications with TU Darmstadt. Piston top T = 675 K, piston side T = 440 K, head T = 500 K, liner temperature 440 K.

The main points of the fired OP E are

- Fuel: methane
- 2500 RPM, relative AFR = 1.0, CR = 8.7
- Mean intake and exhaust pressures 0.95 bar and 1.0 bar, respectively
- Spark timing: 32.8 degrees BTDC

The pressure traces from the computed cycles of fired OP E, functioning as a baseline for HT comparisons, are shown in Figure 39.

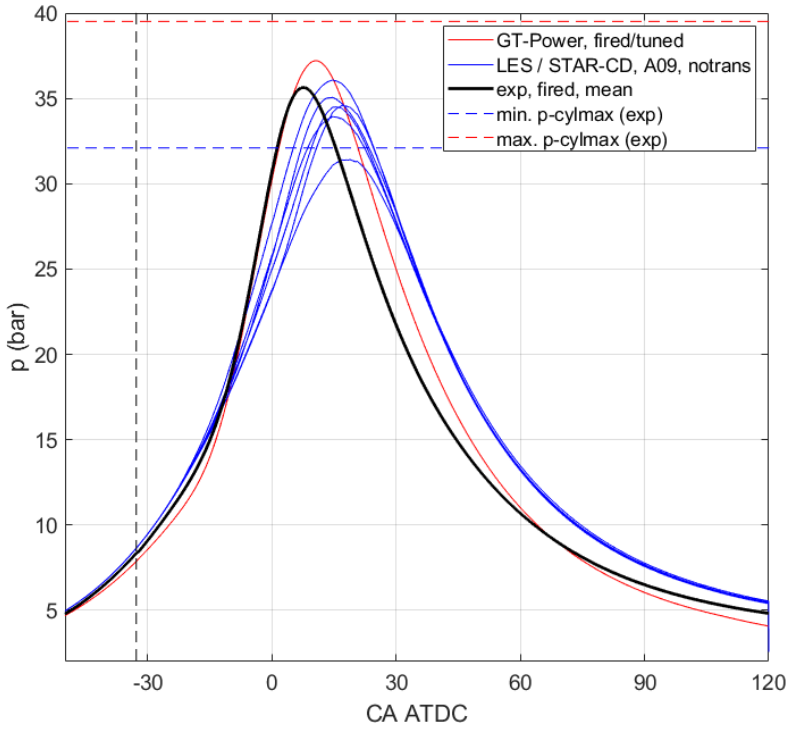

Figure 39. Pressure traces from multi-cycle OP E (fired) against experiments and GT-Power.

3.6.1 Heat flux phenomenology – flame-wall impingement

The reactive DNS of the previous project yielded phenomenological observations of the wall heat flux during flame-wall interaction (Figure 40). Specifically, head-on quenching was associated with a local, high heat flux peak (Figure 40, a), while flame propagation along the wall resulted in high heat flux values along this propagating front (Figure 40, b). It was also noted that heat flux values decreased significantly in the burned gas region ((Figure 40, c).

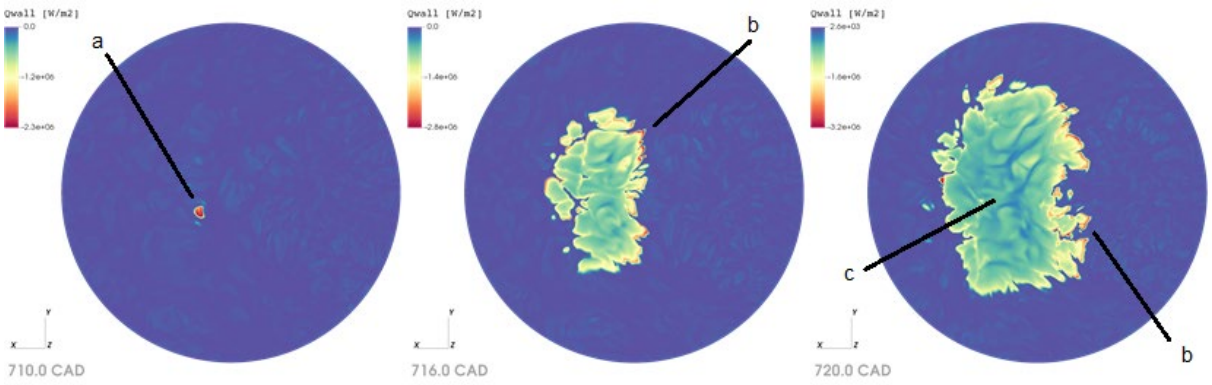

Figure 40. Heat fluxes recorded from previous DNS of fired OP B. The figure shows distinct regions of (a) head-on impingement, (b) side-wall quenching, as well as (c) a distinctly lower heat flux in the remaining burned gas region.

The two wall HT models (ALG & PR) generally performed well in the non-reactive cases, and could be well-compared with the WRLES of OP E. In the reactive cases, more qualitative comparisons are made, since quantitative reference data on wall heat fluxes is not available. Figure 41 shows an instantaneous wall heat flux comparison between the ALG and PR models on the cylinder head.

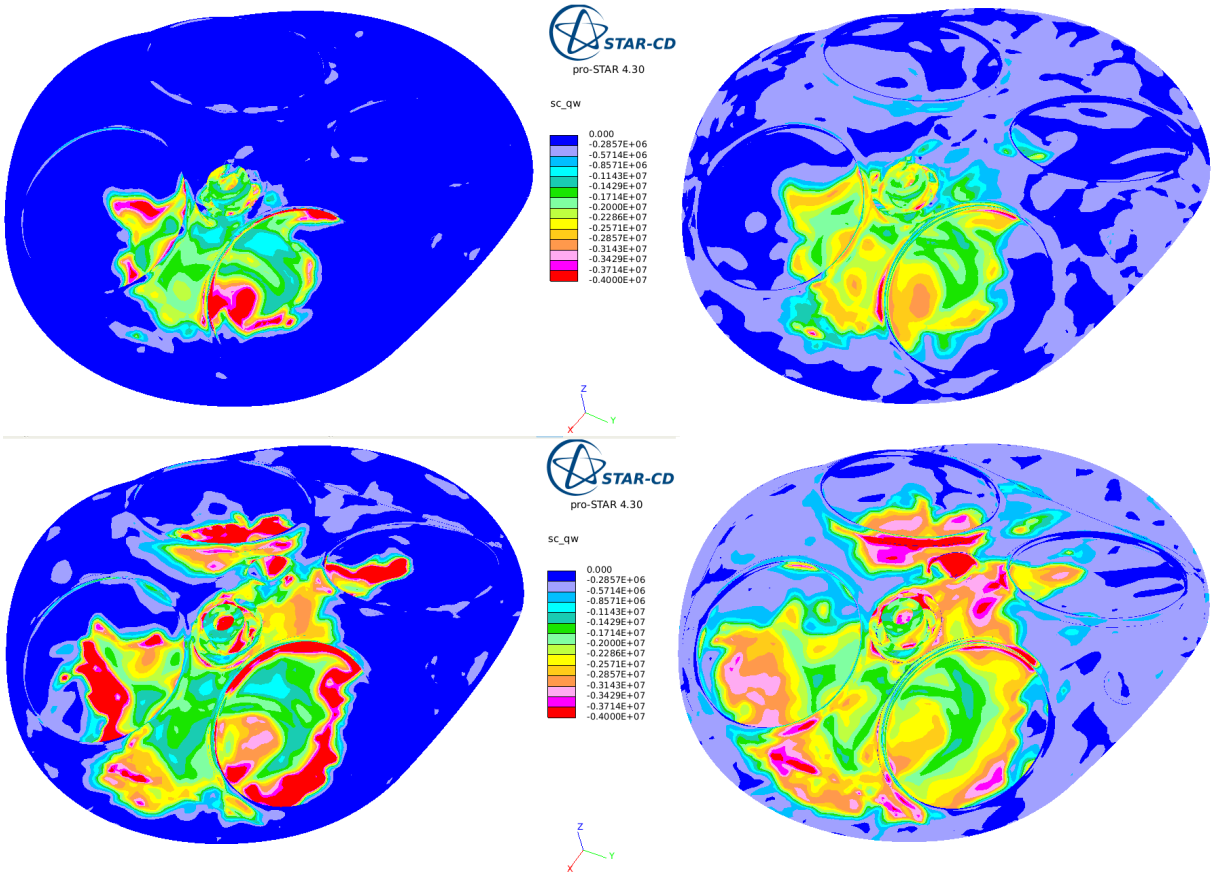

Figure 41. Cylinder head heat flux comparison between the Algebraic model (top) and the PR model (bottom) at 720 (top) and 730 (bottom) degrees CA.

In general, both models result in fairly consistent mean HT levels, but the footprint of the advancing flame-wall interaction is different. For the ALG model, clear high heat flux regions characteristic of side-wall quenching can be noted, meaning that the highest heat transfer occurs at the vicinity of the advancing flame front. In contrast, HT values for the PR model are much more homogeneous in the burned region. The high heat fluxes in regions of side-wall quenching are represented also in the fired DNS of OP B (Figure 40). The high contrast represented by the ALG model is more in line with the DNS results at the significantly different conditions of OP B. However, since quantitative references do not exist for this case, this remains only a hypothesis.

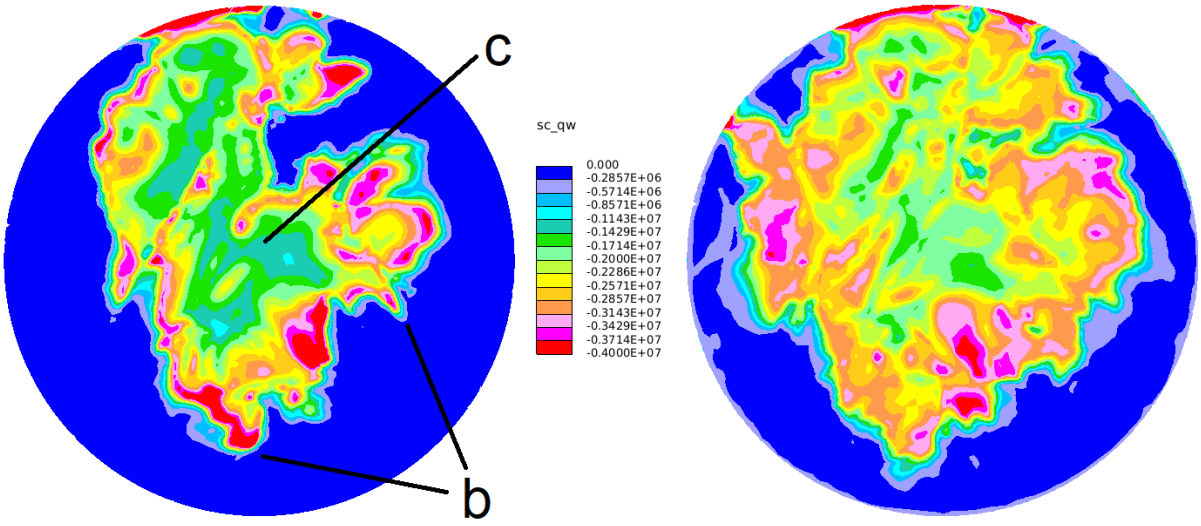

Figure 42. Piston top heat flux comparison between ALG (left) and PR (right) models. The figure highlights regions where the ALG model reproduces phenomenology that is qualitatively correspondent with the DNS, such as side-wall quenching (b) and a considerably lower residual heat flux (c).

It is also prudent to discuss other factors affecting the wall heat flux, besides the wall heat transfer model. First, the present context of a level-set tracking method (G-equation) which takes as input unburned temperature, composition and temperature, does not otherwise take into account nearby enthalpy loss in the vicinity of the walls. While this approach is then uncoupled, a model is in place for near-wall combustion that functions as a transition from turbulent to laminar flame speed, as previously employed in e.g. [24]. Since the transition model involves additional user inputs, it is informative to look at their impact, in comparison with the impact of the WHT model. The near-wall turbulent flame speed $s_{T,nw}$ is determined by

$$s_{T,nw} = s_L + w(s_T - s_L) \tag{10}$$

where w is a Wiebe function

$$w = 1 - \exp\left[-6.908\left(\frac{d_q}{d_w}\right)^{m+1}\right] \tag{11}$$

with d_w being the wall distance and d_q the quenching distance

$$d_q = f_q\left[11.5\mu/\left(C_\mu^{1/4}\rho k_{sgs}^{1/2}\right)\right] \tag{12}$$

where $f_q = 5.0$ is a model parameter, μ is molecular viscosity, $C_\mu = 0.09$, and k_{sgs} is the subgrid turbulent kinetic energy. Figure 43 displays how heat fluxes change when the quenching model is switched off, and when the model constant f_q is doubled. The impact of the wall-quenching model is significant' and of the order of magnitude of the wall heat transfer model at the flame front. For further, detailed development of WMLES WHT models in fired conditions, experimental data such as temporally-resolved heat flux measurements would be valuable. Moreover, additional effort should be invested on high-resolution fired LES computations.

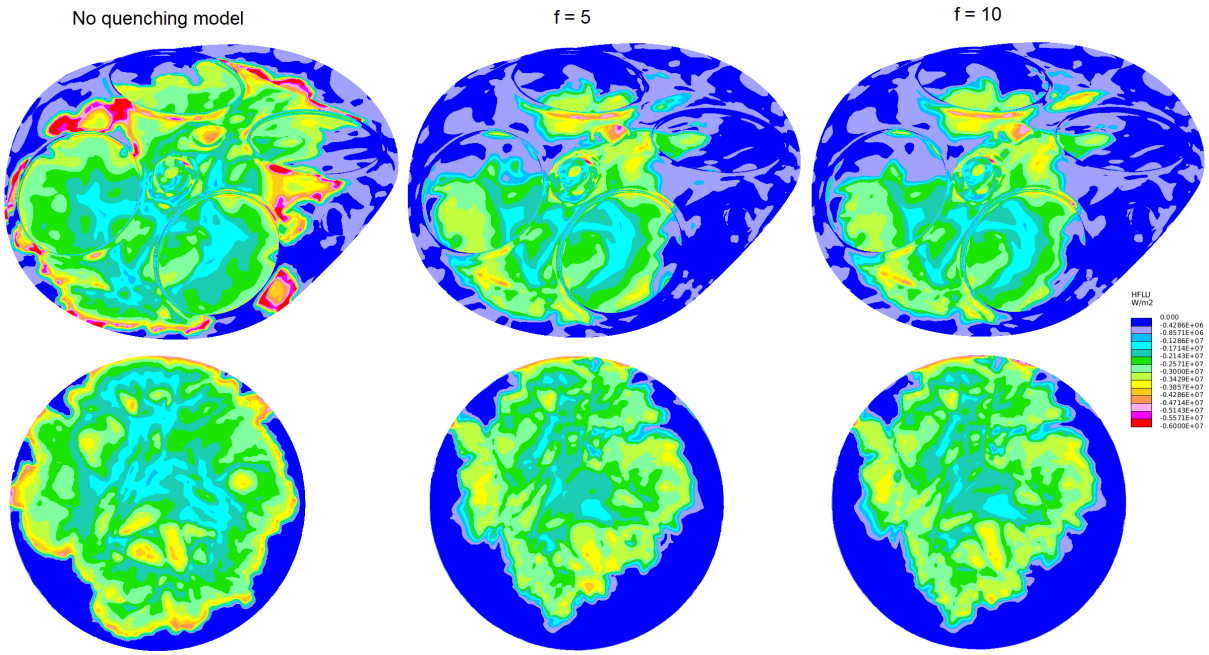

Figure 43. Cylinder head (top) and piston top (bottom) heat fluxes during flame propagation at 730 CA. PR heat transfer model without quenching model (left), f_q = 5.0 (centre), f_q = 10.0 (right)

4 Conclusions

Employing the workflow established in our previous project “Improved description of heat transfer from in-cylinder gases to combustion chamber walls in spark ignition premixed Otto engines”, cutting-edge laser-optical experiments and high-fidelity numerical simulations were extended to the engine-relevant conditions of 2500 RPM in unthrottled conditions. The goals of the project were specifically to extend the physical observations made in the previous work, where boundary layers were found to deviate considerably from ideal flow assumptions. Another question concerned the role and more general applicability of wall heat transfer models in different operating conditions. Multi-cycle WMLES simulations were carried out in several operating points, validated with PIV measurements. As an additional component added to the project, a high-resolution wall-resolved LES (WRLES) was carried out for one compression stroke with similar computational intensity as our previous DNS. The following conclusions are drawn on the basis of the present results.

- Multi-cycle wall-modelled LES of motored OPs A (800 RPM / 0.95 bar), C (1,500 RPM / 0.95 bar), and E (2,500 RPM / 0.95 bar) were carried out and compared with PIV. Engineering-relevant resolutions (0.75-1.0 mm) appear to be sufficient for a good mean flow characterisation for all operating conditions. Result fidelity, quantified by the relevance and magnitude indices, was not strongly impacted by the load/speed (Reynolds number).

- The WRLES for OP E demonstrated similar flow features as the DNS OP B, but with considerably finer turbulent flow structures and higher uniformity of temperature due to better mixing.

- On the piston surface, in both OPs B and E, the boundary layers (BLs) are in a developing state, but at higher Reynolds numbers (OP E), the BLs appear to be better developed. The velocity and thermal BLs do not generally conform to canonical laws of the wall, although the agreement appears to improve at higher load / engine speed.

- The non-dimensional scaling for momentum and thermal BLs, describing the applicability of a “wall function” based on the scaling, changes with (a) the spatial coordinate as the boundary layers develop, (b) time/crank angle, and (c) the engine operating condition. It seems therefore doubtful that any simple wall model based on such scaling can capture the wall stresses and heat fluxes accurately.

- The previously developed algebraic heat transfer (HT) model generated using DNS data was successfully benchmarked against DNS (OP B) and WRLES (OP E) using the Star-CD code. Good global results for both the PR and ALG models were obtained, whereas the dynamic changes in predictions and component-wise results advocated the ALG model. Considering the drastically different scenarios (including reactive conditions) used to develop the ALG model, the good results suggest flexible applicability in various engine conditions. It is notable that the ALG HT model is completely independent of a wall stress model, unlike most models in the literature.

- In fired conditions, the high heat flux maxima characteristic to head-on impingement and side-wall quenching are qualitatively more distinctly represented with the ALG HT model. Besides HT models, treatment of flame-wall interaction is impactful e.g. via near-wall flame speed modelling. In order to enable more quantitative comparisons, wall heat flux measurements should be performed at distinct locations in the combustion chamber. Concurrently, numerical tools should be developed for enhanced high-fidelity computations in the near-wall region, akin to the reactive DNS performed in the previous project.

5 Outlook

The completion of this project marks, to the best of our knowledge, the first wall-resolved computation in a real engine geometry at high load/rpm conditions. On the DNS and high-fidelity LES side, the project is a continuation of a multi-year work to develop highly-efficient and accurate solvers based on the spectral element for the simulation of flow and combustion in engine-like [21, 33], engine-relevant [34] and laboratory-scale engine geometries [5] funded by SNSF, SCCER Mobility, SFOE and the Research Association Combustion Engines FVV e.V. While the generated WRLES data are less resolved than DNS, the numerical resolution of the solutions facilitates their extensive use in further data collection, processing and modelling efforts.

This work continues in the framework of the H2020 project Center of Excellence in Combustion (CoEC), a collective effort of 11 European groups to exploit exascale computing technologies in order to address fundamental challenges related to combustion technologies and support the decarbonization goals of the European Union in the Energy and Transportation sectors. Within this project ETHZ will further develop NekRS, an exascale ready next-generation code, the successor of the spectral element solver Nek5000 targeting extreme-scale computing on multicore and many-core systems as well as graphics processing units.

Reactive flows in fired conditions represent a further, highly relevant target for engineering applications for which wall heat transfer modelling cannot be quantified with the methods available in the present project. Advances in this field would benefit greatly from dedicated wall heat flux and thermal boundary layer measurements at targeted locations in combination with wall-resolved Large-Eddy Simulations. The availability of highly resolved near-wall flame structure, thermal boundary layer information as well as heat flux information are considered instrumental to the development of improved (near-wall) combustion and heat transfer models. This is particularly important in view of future fuels with considerably higher (H_2) or lower (NH_3) reactivity, affecting the flame structure, quenching distance and thereby also the wall heat transfer. A proposal for a follow-up project has therefore been submitted to FVV and the Swiss Federal Office of Energy under the CORNET umbrella. The proposed investigations will be jointly performed between TU Darmstadt (optical engine high-fidelity experiments), ETH Zurich (DNS and wall-resolved LES) and Empa (wall-modelled LES, in collaboration with Aalto University). FVV own contributions for Empa/ETH have already been approved/reserved, conditional on the approval of the overarching CORNET proposal.

6 National and international cooperation

The computational work at LAV was performed in close collaboration with the Reactive Flows and Diagnostics group (RSM) at Technische Unversität Darmstadt, where the motored and fired engine experiments were carried out.

The combined project was co-financed and managed on the German side by the FVV Research Association Combustion Engines (Forschungsvereinigung Verbrennungskraftmaschinen e.V.).

7 Communication

A part of the work was presented at the 2020 Darmstadt Engine Workshop. GT-Power simulations developed during the project were presented at the SAE World Congress, 2020 (SAE Technical Paper 2020-01-0792, cf. below). The final report for the co-funding FVV project 1260 *"Experimentally Validated LES Models for Wall Heat Transfer in Otto Engines"* [35] was presented at the FVV Autumn Conference held at the Nürburgring, Germany, November 8th, 2021. A presentation was further given at the Conference on Combustion research in Switzerland, held at ETH Zurich, September 17th, 2021, jointly organized by the Swiss Federal Office of Energy, ETH and PSI.

8 Publications

Welch et al. *"The Effects of Intake Pressure on In-Cylinder Gas Velocities in an Optically Accessible Single-Cylinder Research Engine"*. No. 2020-01-0792. SAE Technical Paper, 2020.

Bolla et al. *"Development of an algebraic wall heat transfer model for LES in IC engines using DNS data"*, Proceedings of the Combustion Institute **38**: 5811-5819, 2020.

Impagnatiello et al. *"Systematic assessment of data-driven approaches for wall heat transfer modelling for LES in IC engines using DNS data"*, Int. J. Heat Mass Transfer, **183**: 122109, 2022.

Giannakopoulos et al. *"Characterizing the evolution of boundary layers in IC engines by combined laser-optical diagnostics, direct numerical and large-eddy simulations",* in preparation for Flow, Turbulence and Combustion.

Keskinen et al., *"On Reynolds number effects in near-wall engine flows using DNS and wall-resolved LES",* publication in preparation.

Keskinen et al. *"Wall heat transfer models in WMLES: benchmarking against DNS and WRLES in an optical engine"*, publication in preparation.

9 References

1. Keskinen, K., et al., *Final report FVV project 1208 "Wall Heat Transfer in Otto Engines"*. 2020: FVV e.V.
2. Giannakopoulos, G.K., et al., *Final report Swiss Federal Office Of Energy project "Improved description of heat transfer from in-cylinder gases to combustion chamber walls in spark ignition premixed Otto engines", grant no. SI/501615-01*. 2019, Swiss Federal Office Of Energy.
3. Bolla, M., et al., *Development of an algebraic wall heat transfer model for LES in IC engines using DNS data.* Proceedings of the Combustion Institute, 2021. **38**(4): p. 5811-5819.
4. Plengsaard, C. and C. Rutland, *Improved engine wall models for large eddy simulation (LES)*. 2013, SAE Technical Paper.
5. Giannakopoulos, G.K., et al., *LES of the Gas-Exchange Process Inside an Internal Combustion Engine Using a High-Order Method.* Flow, Turbulence and Combustion, 2020. **104**(2): p. 673-692.
6. Negi, P., P. Schlatter, and D. Henningson. *A re-examination of filter-based stabilization for spectral-element methods*. 2017.
7. Fischer, P.F., L. J.W., and S.G. Kerkemeier. *Nek5000 Web page, http://nek5000.mcs.anl.gov*. 2008; Available from: http://nek5000.mcs.anl.gov.
8. Dreizler, A., et al. *Improved description of heat transfer from in-cylinder gases to combustion chamber walls in spark ignition premixed Otto engines*. in *FVV Spring Conference 2020*. 2020. Würzburg: FVV.
9. Deville, M.O., P. Fischer, and E.H. Mund, *High-order methods for incompressible fluid flow*. 2002: Cambridge University Press.
10. Tomboulides, A., J. Lee, and S. Orszag, *Numerical simulation of low Mach number reactive flows.* Journal of Scientific Computing, 1997. **12**(2): p. 139-167.
11. Schmitt, M., *Direct numerical simulations in engine-like geometries*. 2015, ETH Zurich: PhD thesis ETH Nr. 22284.
12. Welch, C., et al., *The Effects of Intake Pressure on In-Cylinder Gas Velocities in an Optically Accessible Single-Cylinder Research Engine*. 2020, SAE Technical Paper.
13. Buhl, S., et al., *A combined numerical and experimental study of the 3D tumble structure and piston boundary layer development during the intake stroke of a gasoline engine.* Flow, Turbulence and Combustion, 2017. **98**(2): p. 579-600.
14. Liu, K. and D.C. Haworth, *Development and assessment of POD for analysis of turbulent flow in piston engines*. 2011, SAE Technical Paper.
15. Hasse, C., V. Sohm, and B. Durst, *Detached eddy simulation of cyclic large scale fluctuations in a simplified engine setup.* International Journal of Heat and Fluid Flow, 2009. **30**(1): p. 32-43.
16. Spalart, P.R., *Detached-eddy simulation.* Annual review of fluid mechanics, 2009. **41**: p. 181-202.
17. di Mare, F., R. Knappstein, and M. Baumann, *Application of LES-quality criteria to internal combustion engine flows.* Computers & Fluids, 2014. **89**: p. 200-213.
18. Choi, H. and P. Moin, *Grid-point requirements for large eddy simulation: Chapman's estimates revisited.* Physics of fluids, 2012. **24**(1): p. 011702.
19. *TRELIS v16.5*. Available from: https://www.csimsoft.com/trelis-cfd.
20. Schroeder, W., K. Marti, and B. Lorensen, *The Visualization Toolkit*. 4th ed. ed. 2006: Kitware.
21. Schmitt, M., et al., *Direct numerical simulation of the effect of compression on the flow, temperature and composition under engine-like conditions.* Proceedings of the Combustion Institute, 2015. **35**(3): p. 3069-3077.
22. Masouleh, M.G., et al., *Modeling cycle-to-cycle variations in spark ignited combustion engines by scale-resolving simulations for different engine speeds.* Applied Energy, 2019. **250**: p. 801-820.

23. Masouleh, M.G., et al., *Flow and thermal field effects on cycle-to-cycle variation of combustion: scale-resolving simulation in a spark ignited simplified engine configuration.* Applied energy, 2018. **230**: p. 486-505.
24. Koch, J., et al., *Reactive computational fluid dynamics modelling methane–hydrogen admixtures in internal combustion engines part II: Large eddy simulation.* International Journal of Engine Research, 2020: p. 1468087420910348.
25. Renaud, A., et al., *Experimental characterization of the velocity boundary layer in a motored IC engine.* International Journal of Heat and Fluid Flow, 2018. **71**: p. 366-377.
26. Hattori, H. and Y. Nagano, *Direct numerical simulation of turbulent heat transfer in plane impinging jet.* International Journal of Heat and Fluid Flow, 2004. **25**(5): p. 749-758.
27. Keskinen, K., et al., *Numerical assessment of wall modelling approaches in scale-resolving in-cylinder simulations.* International Journal of Heat and Fluid Flow, 2018. **74**: p. 154-172.
28. He, C., et al., *Analysis of in-cylinder flow field anisotropy in ic engine using large eddy simulation.* Flow, Turbulence and Combustion, 2017. **99**(2): p. 353-383.
29. Nguyen, T., et al., *Large eddy simulation of an internal combustion engine using an efficient immersed boundary technique.* Flow, Turbulence and Combustion, 2016. **97**(1): p. 191-230.
30. Peters, N., *The turbulent burning velocity for large-scale and small-scale turbulence.* Journal of Fluid Mechanics, 1999. **384**: p. 107-132.
31. Yu, Y., D. Splitter, and S. Kim. *Predicting Cycle-to-cycle Variations in a Spark-ignition Engine using Multi-cycle Large Eddy Simulation*. in *11th U.S. National Combustion Meeting*. 2019. Pasadena, California: Oak Ridge National Lab.(ORNL), Oak Ridge, TN (United States).
32. Smith, G.P., et al., *GRI-Mech 3.0*. 2000.
33. Schmitt, M., et al., *Direct numerical simulation of multiple cycles in a valve/piston assembly.* Physics of Fluids, 2014. **26**(3): p. 035105.
34. Giannakopoulos, G., et al., *Direct numerical simulation of the flow in the intake pipe of an internal combustion engine.* International Journal of Heat and Fluid Flow, 2017. **68**: p. 257-268.
35. Keskinen, K., et al., *Final report FVV project 1260 "Experimentally Validated LES Models for Wall Heat Transfer in Otto Engines"*. 2021: FVV e.V.